Atmos. Meas. Tech. Discuss., doi:10.5194/amt-2017-64, 2017
Manuscript under review for journal Atmos. Meas. Tech.
Discussion started: 5 April 2017

Atmospheric Measurement Techniques Discussions

Cirrus cloud retrieval with MSG/SEVIRI using artificial neural networks

Johan Strandgren[1], Luca Bugliaro[1], Frank Sehnke[2], and Leon Schröder[2]

[1]Deutsches Zentrum für Luft- und Raumfahrt, Institut für Physik der Atmosphäre, Oberpfaffenhofen, Germany
[2]Zentrum für Sonnenenergie- und Wasserstoff-Forschung Baden Württemberg, Systemanalyse, Stuttgart, Germany

Correspondence to: Johan Strandgren (johan.strandgren@dlr.de)

Abstract. Cirrus clouds play an important role in climate as they tend to warm the Earth-Atmosphere system. Nevertheless they remain one of the largest uncertainties in atmospheric research. To better understand the physical processes of cirrus clouds and their climate impact, enhanced satellite observations are necessary. In this paper we present a new algorithm, CiPS (Cirrus Properties from SEVIRI), that detects cirrus clouds and retrieves the corresponding cloud top height, ice optical thickness and ice water path using the SEVIRI imager aboard the geostationary Meteosat Second Generation satellites. CiPS utilises a set of artificial neural networks trained with SEVIRI thermal observations, CALIOP backscatter products, the ECMWF surface temperature and auxiliary data.

CiPS detects 71 and 95 % of all cirrus clouds with an optical thickness of 0.1 and 1.0 respectively, that are retrieved by CALIOP. Among the cirrus free pixels, CiPS classifies 96 % correctly. With respect to CALIOP, the cloud top height retrieved by CiPS has a mean absolute percentage error of 10 % or less for cirrus clouds with a top height greater than 8 km. For the ice optical thickness, CiPS has a mean absolute percentage error of 50 % or less for cirrus clouds with an optical thickness between 0.35 and 1.8, and of 100 % or less for cirrus clouds with an optical thickness down to 0.07, with respect to the optical thickness retrieved by CALIOP. The ice water path retrieved by CiPS shows a similar performance, with mean absolute percentage errors of 100 % or less for cirrus clouds with an ice water path down to 1.7 g m^{-2}. Since the training reference data from CALIOP only include ice water path and optical thickness for comparably thin clouds, CiPS does also retrieve an opacity flag, which tells whether a retrieved cirrus is likely to be too thick for CiPS to accurately derive the ice water path and optical thickness.

By retrieving CALIOP like cirrus properties with the large spatial coverage and high temporal resolution of SEVIRI during both day and night, CiPS is a powerful tool for analysing the temporal evolution of cirrus clouds including their optical and physical properties. To demonstrate this, the life cycle of a thin cirrus cloud is analysed.

1 Introduction

High level clouds cover 27-37 % of the Earth's surface (Stubenrauch et al., 2013, the exact figure depending on the satellite instrument and its sensitivity to thin and sub-visual cirrus) and do consequently play an important role in the climate system by reflecting the incoming solar radiation and absorbing the outgoing thermal radiation. In this study we focus on cirrus clouds,

Atmos. Meas. Tech. Discuss., doi:10.5194/amt-2017-64, 2017
Manuscript under review for journal Atmos. Meas. Tech.
Discussion started: 5 April 2017

Atmospheric Measurement Techniques Discussions

defined as all clouds that consist of ice crystals. In general, the net cirrus radiative forcing is strongly depending on the position and thickness of the cloud as well as the microphysical properties like ice crystal shape, size distribution and ice water content (e.g. Fu and Liou, 1993; Zhang et al., 1999; Liou, 2002; Wendisch et al., 2007). Because of the tenuous nature of cirrus clouds the reflection of solar radiation can be outweighted by the thermal effect (Meerkötter et al., 1999) leading to a positive net radiative forcing, as is the case for thin cirrus (Jensen et al., 1994; Chen et al., 2000). Despite the constant progress in cirrus research and the continuous development of more advanced instruments and retrieval algorithms, the understanding of the physical processes that govern the cirrus life cycle as well as the temporal evolution of their physical and optical properties is still limited, as is their representation in weather and climate models (Waliser et al., 2009; Eliasson et al., 2011).

To capture the temporal evolution throughout the cirrus life cycle as well as the diurnal cycles of cirrus coverage and properties like cloud top height (CTH), ice optical thickness (IOT) and ice water path (IWP), it is essential to accurately and consistently detect and monitor cirrus during both day and night. To this end, imagers like SEVIRI (Spinning Enhanced Visible and Infrared Imager, Schmetz et al., 2002) aboard the geostationary Meteosat Second Generation (MSG) satellites are the instruments of choice since they combine a large field of view with a high temporal resolution.

Cirrus clouds can be detected from space-borne imagers (e.g. Saunders and Kriebel, 1988; Derrien et al., 1993; Ackerman et al., 1998; Kriebel et al., 2003; Derrien and LeGleau, 2005; Krebs et al., 2007) by applying spectral tests on brightness temperatures and temperature differences (e.g. Inoue, 1985; Ackerman et al., 1990). Krebs et al. (2007) extend the multi-spectral threshold test approach by introducing morphological tests that take into account the shape of high level clouds in thermal water vapour observations. Near infrared water vapour absorption channels can also be used to detect cirrus clouds (Gao et al., 2002). Passive imagers do however have a limited sensitivity to thin cirrus clouds and algorithms utilising spectral and morphological threshold tests tend to miss a large fraction of those thin cirrus (e.g. Ackerman et al., 2008; Holz et al., 2008; Stubenrauch et al., 2010) and thus introduce a bias into the climate impact of cirrus clouds. Another well known problem related to cloud detection from passive imagers is the difficulty to distinguish between cirrus clouds and cold surfaces in the polar regions (e.g. Holz et al., 2008).

The CTH is an important variable as it determines the outgoing longwave radiation. It can be retrieved from passive satellite imagers during both day and night using e.g. radiance ratioing (also referred to as CO_2 absorption, CO_2 slicing and split window technique) (Smith et al., 1970; Smith and Platt, 1978; Menzel et al., 1983; Eyre and Menzel, 1989; Zhang and Menzel, 2002; Menzel et al., 2008), radiance fitting (e.g. Szejwach, 1982; Nieman et al., 1993; Schmetz et al., 1993), and optimal estimation (e.g. Heidinger and Pavolonis, 2009; Sayer et al., 2011; Watts et al., 2011). An inter-comparison of different techniques currently used for SEVIRI is presented in Hamann et al. (2014).

Nakajima and King (1990) introduced a commonly applied approach for the retrieval of optical thickness and effective particle radius of clouds from reflected solar radiation in two spectral channels (e.g., Platnick et al., 2003; Bugliaro et al., 2011; Stengel et al., 2014) for both ice clouds and liquid water clouds. From the optical thickness and effective radius the liquid and ice water paths (LWP and IWP respectively) can be estimated for liquid and icy pixels respectively. The solar dependence does however limit this approach to daytime and the retrieval becomes ambiguous for optically thin clouds (Nakajima and King, 1990). The same properties can be retrieved for optically thin cirrus clouds during night as well using only thermal observations

Atmos. Meas. Tech. Discuss., doi:10.5194/amt-2017-64, 2017
Manuscript under review for journal Atmos. Meas. Tech.
Discussion started: 5 April 2017

Atmospheric Measurement Techniques Discussions

(e.g. Prabhakara et al., 1988; Ackerman et al., 1990; Yue and Liou, 2009; Minnis et al., 2011; Heidinger et al., 2015; Wang et al., 2016), but with a limited accuracy due to the low sensitivity to large ice crystal sizes and large optical thicknesses.

The limited amount of vertical information and sensitivity to thin cirrus clouds is a recurrent drawback of passive imagers. The spaceborne lidar CALIOP (Cloud-Aerosol Lidar with Orthogonal Polarization, Winker et al., 2009), measures profiles of attenuated backscatter with a vertical resolution of up to 30 m and is currently the most accurate source for the detection of cirrus clouds and the retrieval of their top height and optical thickness from space. CALIOP is an active sensor and can consequently operate during both day and night but the small spatial scale and the repeat cycle of approx. 16 days make it inadequate for studying the temporal evolution of cirrus clouds.

As an attempt to combine the advantages from a polar orbiting lidar and a geostationary imager, Kox et al. (2014) present an approach for the detection and retrieval of optical thickness and top height of cirrus clouds from SEVIRI. Their algorithm COCS (Cirrus Optical properties from CALIOP and SEVIRI) utilises an artificial neural network (ANN) trained with coincident CALIOP backscatter and SEVIRI thermal observations in order to estimate CALIOP-like cirrus properties from SEVIRI. During the training procedure the ANN learns to generalise, such that it can estimate a desired output vector for a set of previously unseen input data. This together with the low computational costs makes neural networks an interesting alternative to more commonly used physically based methods. Minnis et al. (2016) present a similar approach to estimate the optical thickness of opaque ice clouds at night using an ANN trained with coincident CloudSat/CPR (Cloud Profiling Radar) measurements and Aqua/MODIS (Moderate Resolution Imaging Spectroradiometer) infrared radiances. Holl et al. (2014) use combined CALIPSO/CALIOP and CloudSat/CPR retrievals for the retrieval of the IWP from AVHRR (Advanced Very High Resolution Radiometer) and MHS (Microwave Humidity Sounder) on the NOAA and MetOp satellites using neural networks. Cerdena et al. (2006, 2007) use neural networks trained with simulated radiances for the retrieval of optical thickness, effective radius and temperature of liquid water clouds (day and night) and cirrus clouds (only day) from NOAA/AVHRR. Taravat et al. (2015) use neural networks for the daytime cloud detection from SEVIRI.

In this paper we present CiPS (Cirrus Properties from SEVIRI), a new algorithm for cirrus remote sensing with SEVIRI that exploits the basic idea of COCS: retrieving cirrus properties using ANNs trained with CALIOP and SEVIRI data. However, CiPS clearly differs from COCS in the implementation of this idea and the achieved performance. For a more accurate cirrus detection and determination of CTH and IOT, CiPS utilises a different set of input parameters including numerical weather model data and information about nearby pixels. In addition, CiPS classifies each pixel as either cirrus free, transparent cirrus or opaque cirrus by means of dedicated classification ANNs. As CALIOP gets saturated for thicker clouds, the opacity information is an important additional information in order to better characterise the cirrus and the reliability of the ANN results that was absent in COCS. Furthermore, CiPS is trained to retrieve the IWP, resulting in a total of three climate relevant cirrus cloud properties that can be estimated during both day and night for the full SEVIRI field of view every 15 minutes. In particular, the IWP retrieved by CiPS allows for a direct comparison with climate, weather and LES models. CiPS targets thin cirrus clouds, as those clouds are most difficult to retrieve using thermal satellite observations from geostationary orbits. The more thin cirrus clouds that can be detected and accurately retrieved, the smaller the bias of the derived radiative forcing and climate impact of cirrus clouds will be. Thus CiPS helps to fill this gap of observations in cloud remote sensing.

Atmos. Meas. Tech. Discuss., doi:10.5194/amt-2017-64, 2017
Manuscript under review for journal Atmos. Meas. Tech.
Discussion started: 5 April 2017

Atmospheric Measurement Techniques Discussions

The remainder of this paper is divided into five parts. In Sect. 2 the instruments, data and tools used for this study are introduced and described. The new algorithm, CiPS, is described in detail in Sect. 3. Section 4 shows the performance of CiPS for a SEVIRI scene over parts of Europe together with a detailed validation of all quantities using CALIOP as reference. To illustrate the capability and performance of CiPS, a life cycle analysis of a thin cirrus cloud using CiPS is presented in Sect. 5. Finally the performance of CiPS is shortly summarised and discussed in the concluding section. A list of abbreviations is available in Appendix A.

2 Instruments and tools

2.1 SEVIRI

SEVIRI is a passive imager operating aboard the geostationary Meteosat Second Generation (MSG) satellites operational since 2004. SEVIRI has a sampling distance of 3 km at nadir (1 km for the broadband visible channel) and a temporal resolution of 15 min. Limiting the spatial coverage to the upper part of the SEVIRI disc (north of approx. 15° N), the temporal resolution can be increased to 5 min using the rapid scanning service. SEVIRI measures photon counts in twelve wavelength intervals (Schmetz et al., 2002), from which the radiances, reflectances and equivalent black body brightness temperatures can be derived.

2.2 CALIOP

CALIOP was launched as the main instrument aboard the CALIPSO (Cloud-Aerosol Lidar and Infrared Pathfinder Satellite Observations) satellite in 2006. CALIPSO is flying in a sun-synchronous orbit as part of the A-Train (Stephens et al., 2002). CALIOP is an elastic backscatter lidar operating at 2 wavelengths, 532 and 1064 nm. The frequency of 20.16 Hz produces a ∼70 m footprint, every 335 m on the Earth's surface, resulting in curtains of attenuated backscatter profiles along the CALIPSO track (Winker et al., 2009). A long set of algorithms are applied to the backscatter profiles in order to detect cloud and aerosol layers (Vaughan et al., 2009), differentiate between the two (Liu et al., 2009), determine the cloud phase (Hu et al., 2009) and finally derive profiles of volume extinction coefficients (Young and Vaughan, 2009). For the cloudy regions where the cloud phase is determined to be ice, the ice water content (IWC) is calculated from the retrieved extinction coefficients using a parametrisation derived by Heymsfield et al. (2005) based on extensive in situ measurements. The layer IOT and IWP is obtained by integrating the vertical profiles of extinction coefficients and IWC.

The CALIOP retrieved cirrus properties have been validated using in situ and CPL measurements. CPL McGill et al. (Cloud Physics Lidar, 2002) is an airborne high spectral resolution lidar with a higher signal-to-noise ratio, higher vertical and horizontal resolution and lower multiple scattering compared to CALIOP. Yorks et al. (2011) show that CALIOP and CPL agree on 90 % of the scene classifications (cirrus or no cirrus) on average with an excellent agreement in cloud top height. The CALIOP retrieved optical thickness is on average 15 % above the CPL optical thickness (Hlavka et al., 2012). The IWC derived from the CALIOP extinction coefficients shows generally good agreement with in situ measurements. Below 12 km

Atmos. Meas. Tech. Discuss., doi:10.5194/amt-2017-64, 2017
Manuscript under review for journal Atmos. Meas. Tech.
Discussion started: 5 April 2017

Atmospheric Measurement Techniques Discussions

CALIOP retrieves lower IWC, whereas above 12 km CALIOP retrieves comparable or higher IWC (Avery et al., 2012). Holz et al. (2016) show that the single layer IOT derived from unconstrained CALIOP retrievals (Young and Vaughan, 2009) is low-biased with respect to a single channel thermal/IR IOT retrieval combining CALIOP/MODIS observations and forward radiative transfer modelling. The bias is shown to increase with increasing IOT.

2.3 Artificial neural networks

An artificial neural network consists of a number of neurons that exchange information with each other, in a similar manner as biological nerve cells transmit information via synapses in the human brain. By assigning each neuron-neuron connection a numeric tunable weight, the ANN has the ability of learning patterns and approximating functions. The goal of an ANN is to derive a vector of unknown output variables given a vector of known input data. This tool is applied in Sect. 2.5 and 3 to the remote sensing of cirrus clouds and is thus introduced in the following.

2.3.1 Multilayer perceptron

In this study a multilayer perceptron (MLP), a feed-forward artificial neural network, is used. A MLP consists of three major units; 1) the input layer, 2) the output layer and 3) the hidden layer(s). The input layer holds as many neurons as input variables and the output layer as many neurons as desired output variables. The hidden layer(s) hold an arbitrary number of additional neurons distributed over an arbitrary number of hidden layers. All connections between the neurons within the MLP are in the forward direction (input layer → hidden layer(s) → output layer). Connections backward or within a layer are forbidden (Rumelhart et al., 1986). The value of a neuron is calculated by processing the output from the preceding neurons connected to that neuron and the corresponding weights through an *activation function*. These non-linear functions allow the ANN to solve complex problems with a limited number of neurons. A generic structure of a MLP is illustrated in Fig. 1. In addition to the input and hidden neurons, a constant bias neuron is commonly added to the input and hidden layers in order to give the MLP more flexibility during the training.

When the MLP is given a vector of input data it uses the connection weights and possible biases to estimate the vector of output data. Thus, it is crucial that the weights are assigned correct values.

2.3.2 Learning through backpropagation

The weights are tuned by training the MLP, which is done with a teacher/trainer approach, more known as supervised training. A commonly used training algorithm is the backpropagation algorithm. The most essential steps in the backpropagation algorithm are explained below, but for the curious reader the algorithm as a whole is well explained in Rumelhart et al. (1986).

Using backpropagation the network is fed with a set of training examples where the vector of input variables as well as the vector of expected output variables are known. From the training input data the MLP estimates its own output data using the current weights. From the vector of *estimated* output and the corresponding vector of *expected* output the total error E (squared difference) is calculated. The error is then propagated backwards through the MLP and used to update each weight

Atmos. Meas. Tech. Discuss., doi:10.5194/amt-2017-64, 2017
Manuscript under review for journal Atmos. Meas. Tech.
Discussion started: 5 April 2017

Atmospheric Measurement Techniques Discussions

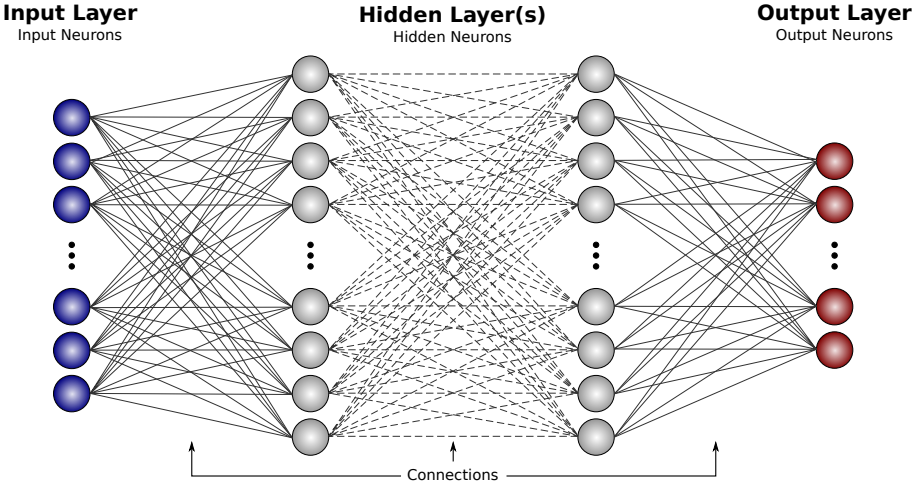

Figure 1. Generic structure of a multi layer perceptron (MLP), a form of a feed-forward artificial neural network used in this study.

using gradient descent in such a way that the total error is minimised. Each weight is updated using the following equation:

$$w_{ij}^{*} = w_{ij} - \eta \frac{\delta E}{\delta w_{ij}} = w_{ij} - \Delta w_{ij} \, . \tag{1}$$

where w_{ij} and w_{ij}^{*} are the old and new values for a weight connecting the two neurons i and j. $\frac{\delta E}{\delta w_{ij}}$ describes how much a change in w_{ij} affects the total error E. To adjust how aggressive the weight updates should be, a *learning rate* η is multiplied with $\frac{\delta E}{\delta w_{ij}}$ before the weight update. A larger learning rate means larger changes in the weights and thus a faster training. This can however lead to an oscillation of the total error around a minimum solution. With a small learning rate the total error will not oscillate around a minimum solution, but the training is slower and the risk of getting stuck in local minima is higher. By introducing a *momentum* term α, possible oscillations in the iterative search for the minimum error are attenuated, and this allows for a larger learning rate. The momentum makes use of the previous update of the corresponding weight in order to get a weighted sum of the current and previous error gradients. The momentum term is added to the second term on the right hand side of Eq. (1) such that

$$\Delta w_{ij}^{k} = \eta \frac{\delta E}{\delta w_{ij}} + \alpha \Delta w_{ij}^{k-1} \, , \tag{2}$$

where k represents the k^{th} update of the weight w_{ij}, meaning that Δw_{ij}^{k-1} is the previous update of weight w_{ij} (Rumelhart et al., 1986).

To find the minimum total error between the estimated and expected output vectors for a complex problem and tune the weights accordingly, a large training dataset is required. Training a MLP is an iterative process, where each training example is presented to the ANN multiple times until a satisfying result has been achieved. With common ANN terminology the training completes one *iteration* every time the weights are updated and one *epoch* when all training examples contained in the training dataset have been presented to the ANN. The amount of iterations required for one epoch does therefore depend on the amount

Atmos. Meas. Tech. Discuss., doi:10.5194/amt-2017-64, 2017
Manuscript under review for journal Atmos. Meas. Tech.
Discussion started: 5 April 2017

Atmospheric Measurement Techniques Discussions

Table 1. Contingency table for the cirrus detection from CALIOP and CiPS.

		CALIOP	
		Cirrus	No cirrus
CiPS	Cirrus	N_{TP}	N_{FP}
	No cirrus	N_{FN}	N_{TN}

of training examples the ANN is given for every update of the weights i.e. the *batch size*. With stochastic gradient descent (sometimes referred to as momentum stochastic gradient descent, when the momentum term is used) the weights are updated for each training example (batch size $= 1$), whereas for full batch gradient descent the weights are updated using all training examples at once (batch size $= N$, where N is the total number of training examples). Stochastic gradient descent leads to a noisy error gradient whereas the full batch gradient descent requires more computational power to converge. With mini-batch gradient descent an intermediate number of training examples is used for each weight update (1 < batch size < N).

While in recent years very potent new learning methods that are based on backpropagation were developed, stochastic gradient descent is still the most used method due to its simplicity and robustness (Schmidhuber, 2015).

2.4 Validation metrics

This section introduces the validation metrics used for the validation later on in this paper.

The probability of detection (POD) is used to measure how efficiently CiPS detects cirrus clouds and is given by

$$\text{POD} = \frac{N_{TP}}{N_{TP} + N_{FN}} , \tag{3}$$

where the number of true positives, N_{TP}, are all points correctly classified as cirrus and the number of false negatives, N_{FN}, all cirrus clouds that remain undetected. The denominator, $N_{TP} + N_{FN}$, is thus the total number of points with a reference cirrus cloud. The false alarm rate (FAR) measures the fraction of cirrus free points that are falsely classified as being cirrus clouds:

$$\text{FAR} = \frac{N_{FP}}{N_{FP} + N_{TN}} . \tag{4}$$

The number of false positives, N_{FP}, are all points falsely classified as cirrus (false alarms) and the number of true negatives, N_{TN}, all points correctly identified as cirrus free. The denominator, $N_{FP} + N_{TN}$, is thus the total number of points with no reference cirrus cloud. The corresponding CALIOP data are used as a reference when calculating the POD and FAR. Table 1 clarifies the quantities used to calculate the POD and FAR. The POD and FAR are also used to measure how effectively CiPS can determine the opacity/transparency of detected cirrus clouds.

Atmos. Meas. Tech. Discuss., doi:10.5194/amt-2017-64, 2017
Manuscript under review for journal Atmos. Meas. Tech.
Discussion started: 5 April 2017

Atmospheric Measurement Techniques Discussions

The mean percentage error (MPE) and mean absolute percentage error (MAPE) are used to measure the accuracy of the CTH, IOT and IWP retrievals with respect to CALIOP. The MPE is given by

$$\mathrm{MPE} = \frac{100\%}{N} \sum_{i=1}^{N} \frac{E_i - O_i}{O_i}, \tag{5}$$

where O is the observed value by CALIOP and E the estimated value by CiPS and the sum spans over all samples $i = 1, \ldots, N$ used for the evaluation. The MPE gives information about the direction of the deviations, i.e. whether CiPS tends to overestimate (positive MPE) or underestimate (negative MPE) the values with respect to CALIOP. The MAPE is given by

$$\mathrm{MAPE} = \frac{100\%}{N} \sum_{i=1}^{N} \left| \frac{E_i - O_i}{O_i} \right|, \tag{6}$$

and gives information about the average magnitude of the errors relative to the expected values observed by CALIOP. A vanishing MAPE means no deviation from the observed values and a perfect correlation.

2.5 The COCS algorithm

The COCS (Cirrus Optical properties from CALIOP and SEVIRI) algorithm retrieves CTH and IOT of cirrus clouds from SEVIRI (Kox et al., 2014). It combines V2 CALIOP L2 cloud layer data, SEVIRI thermal observations and auxiliary data using an ANN to retrieve CALIOP-like cirrus properties for the full SEVIRI field of view every 15 min and 24 h per day. The cirrus properties retrieved with COCS are used for comparison with CiPS in Sect. 4.2 and COCS is thus shortly introduced here.

COCS is a MLP with ten input neurons (7 brightness temperatures and temperature differences, viewing zenith angle, land-sea mask and latitude), two output neurons (IOT and CTH) and 600 neurons in one single hidden layer. COCS was trained with three years of data including SEVIRI observations from both MSG-1 and MSG-2. The detection of cirrus clouds takes place indirectly in COCS: a pixel is cirrus covered if its IOT ($\mathrm{IOT_{COCS}}$) ≥ 0.1, meaning that pixels with $\mathrm{IOT_{COCS}} < 0.1$ are considered too uncertain and regarded as cirrus free. The value of 0.1 was chosen as a trade-off between high POD and low FAR.

The V2 CALIOP L2 cloud layer products contain no information on data quality and the feature classification flag and feature optical thickness among other variables were released as beta products (early release). CALIOP V2 layer data used in Kox et al. (2014) had to fulfil three filtering conditions to be classified as a cirrus cloud: 1) To exclude inaccurate retrievals due to diverging extinction retrievals in opaque cloud layers, the maximum IOT was limited to 2.5. 2) To ensure that the cirrus clouds were not falsely classified layers of aerosols or liquid water clouds, the mid-layer temperature had to be 243 K or colder. 3) The layer top height had to exceed 9.5 km in the tropics and 4.5 km in polar regions, with a linear decrease between these two values in mid-latitudes.

Atmos. Meas. Tech. Discuss., doi:10.5194/amt-2017-64, 2017
Manuscript under review for journal Atmos. Meas. Tech.
Discussion started: 5 April 2017

3 CiPS

CiPS is the new algorithm, based on the heritage from COCS in the sense that it also utilises artificial neural networks primarily trained with SEVIRI and CALIOP data. Significant enhancements with regards to the ANN structure, training input and output data and training methodology have been implemented though, in order to improve on retrieval performance and computational speed. In addition to CTH and IOT, CiPS is also trained to retrieve cloud opacity information and the IWP.

3.1 Multiple artificial neural networks

In contrast to COCS that uses one single ANN to retrieve IOT and CTH, CiPS utilises four ANNs, making it possible to customise the input variables, training data and ANN structures individually for each task to be solved.

1. The first ANN is a classification network trained to detect cirrus clouds using a binary cirrus cloud flag (CCF). Due to the continuous activation function used by the ANN (Sect. 2.3.1), the retrieved value of the CCF neuron is a decimal number (0–1) that can be seen as a cirrus probability, where high and low values indicate a high and low probability of cirrus presence respectively. This provides at least three major advantages over an IOT threshold based detection: 1) The CCF detection threshold (0–1) can be determined depending on the application. A higher threshold means a lower FAR, whereas a lower threshold means a higher POD (Eq. (3)). 2) The cirrus detection is independent of the IOT and not limited to cirrus clouds with an estimated optical thickness greater than 0.1, as is the case for COCS. 3) Since no additional information is needed for the pixels classified as cirrus free by the cirrus detection ANN, the ANNs for CTH, IOT, IWP and opacity information retrieval can be trained only with cases where cirrus clouds are present. This excludes a large number of largely different input data combinations representing the same "cirrus" properties, i.e. the situations where IOT=IWP=0.

2. The second ANN is used for the CTH retrieval.

3. The third ANN is used for the IOT/IWP retrieval. These two variables are provided by the same network since they are physically closely related (Heymsfield et al., 2005).

4. CALIOP cannot provide accurate IOT/IWP retrievals for thicker cirrus clouds where the laser beam is completely attenuated. Hence the estimated IOT and IWP by CiPS for such situations should not be trusted. Therefore a second classification network is introduced with CiPS, trained to identify the cirrus clouds where CALIOP is saturated. Similarly to the cirrus detection ANN, the opacity classification ANN retrieves values between 0–1, that can be regarded as an opacity probability information. From here a binary opacity flag (OPF) is obtained using a suitable opacity classification threshold (Sect. 3.6).

3.2 Input data

The following subsections introduce all input data used to train CiPS. An overview is provided in Tab. 2.

Atmos. Meas. Tech. Discuss., doi:10.5194/amt-2017-64, 2017
Manuscript under review for journal Atmos. Meas. Tech.
Discussion started: 5 April 2017

Atmospheric Measurement Techniques Discussions

3.2.1 Brightness temperatures from SEVIRI

Brightness temperatures derived from the photon counts in all thermal channels of SEVIRI except for the ozone channel at 9.7 µm are used. The ozone channel is excluded because its sensitivity peaks in the stratosphere, where no cirrus clouds are present, and because of its strong annual cycle due to the ozone variability (Ewald et al., 2013). Channels with significant solar contribution are excluded in order to have the same conditions and similar performance during both day and night. Alongside the single brightness temperatures, CiPS works pixel by pixel and takes advantage of the information from nearby pixels by utilising the regional *maximum* brightness temperatures for the 3 window channels centred at 8.7, 10.8 and 12.0 µm. The regional maximum temperature is identified for each pixel as the maximum temperature within a 19×19 pixels large box centred at the pixel under consideration. The idea with the regional maximum brightness temperature is to estimate the temperature that SEVIRI would observe for a cirrus covered pixel if the pixel was cirrus free. This is done by assuming that at least one of the 361 pixels within the box is not covered by a cirrus cloud (Krebs et al., 2007). The corresponding cirrus free temperature is useful both for the detection of cirrus clouds and the retrieval of the cirrus properties since it provides information about the up-welling radiation from the surface or lower water clouds. The box size of 19×19 pixels is chosen such that the region is small enough to reduce the risk of unrepresentative maximum temperatures over inhomogeneous surfaces (e.g. coast lines), but large enough to increase the chance of capturing a representative cirrus free pixel.

For the classification ANNs (CCF and OPF) the regional *average* brightness temperatures for the 2 water vapour channels centred at 6.2 and 7.3 µm are used as well. The regional averaged brightness temperatures are calculated for each pixel as the boxcar average temperature within a 19×19 pixels large box centred at the pixel under consideration. A homogeneous area with cold temperatures indicates the presence of a thick cirrus cloud. The combination of a single temperature and the corresponding regional average for the water vapour channels provides information about high cloud structures useful for the detection of cirrus clouds (Krebs et al., 2007).

3.2.2 Surface temperature from ECMWF

With CiPS we introduce modelled data from the ECMWF ERA-Interim re-analysis dataset (Dee et al., 2011) to the list of input variables. The surface skin temperature T_{surf} is strongly related to the thermal radiation emitted by the Earth and thus related to the brightness temperatures observed by SEVIRI. This information helps accounting for the radiation emitted by the surface which is partly transmitted in the satellite direction through thin cirrus. It also helps the ANNs to distinguish between cirrus clouds and cold surfaces like Greenland and Antarctica. The temporal resolution of 6 h and spatial resolution of 0.125°is used.

3.2.3 Auxiliary data

Along with the data provided by SEVIRI and ECMWF, additional auxiliary datasets are used. The latitude provides valuable information about the geographical location with respect to the global circulation convergence and divergence zones (e.g. the ITCZ, subsidence regions and the polar front) which strongly affect the presence and properties of cirrus clouds. Considering the SEVIRI viewing zenith angle, the SEVIRI pixel size and slant path length are implicitly accounted for. Two flags indicating

Atmos. Meas. Tech. Discuss., doi:10.5194/amt-2017-64, 2017
Manuscript under review for journal Atmos. Meas. Tech.
Discussion started: 5 April 2017

Atmospheric Measurement Techniques Discussions

Table 2. Input data used to train the four ANNs contained in CiPS. BT=Brightness Temperature, regavg=regional average, regmax=regional maximum, VZA=viewing zenith angle.

	CCF	OPF	CTH	IOT/IWP
$BT_{6.2\mu m}$	✓	✓	✓	✓
$BT_{7.3\mu m}$	✓	✓	✓	✓
$BT_{8.7\mu m}$	✓	✓	✓	✓
$BT_{10.8\mu m}$	✓	✓	✓	✓
$BT_{12.0\mu m}$	✓	✓	✓	✓
$BT_{13.4\mu m}$	✓	✓	✓	✓
$BT_{6.2\mu m,\ regavg}$	✓	✓		
$BT_{7.3\mu m,\ regavg}$	✓	✓		
$BT_{8.7\mu m,\ regmax}$	✓	✓	✓	✓
$BT_{10.8\mu m,\ regmax}$	✓	✓	✓	✓
$BT_{12.0\mu m,\ regmax}$	✓	✓	✓	✓
T_{surf}	✓	✓	✓	✓
Latitude	✓	✓	✓	✓
VZA	✓	✓	✓	✓
Water flag	✓	✓	✓	✓
Snow/ice flag	✓	✓	✓	✓
$\sin(2\pi\frac{DOY}{365})$	✓	✓	✓	✓
$\cos(2\pi\frac{DOY}{365})$	✓	✓	✓	✓

the presence of surface water and permanent ice/snow respectively are included to gain additional information about the observed surface type. Due to the seasonal variations in the global circulation and the presence of cirrus clouds (Stubenrauch et al., 2013) the day of the year (DOY) is used. The DOY is converted to two variables, $\sin(2\pi\,\mathrm{DOY}/365)$ and $\cos(2\pi\,\mathrm{DOY}/365)$ in order to remove the hard transition from December 31 to January 1. Two variables are used to avoid the repeating pattern of sine or cosine alone.

3.3 Output data: cirrus properties from CALIOP

The cirrus presence and properties, including a CCF and an OPF as well as the CTH, IOT and IWP are derived from the V3 CALIOP L2 5 km cloud and aerosol layer products (CAL_LID_L2_05kmClALay-Prov-V3-0X..., CALIPSO Science Team, 2016a, b). Major improvements with respect to V2 data include enhanced cloud-aerosol discrimination, improved cloud thermodynamic phase determination, more accurate estimates of layer spatial and optical properties as well as an improved estimate of the low cloud fraction. Furthermore, new products like the IWP and retrieval uncertainties are included. Most importantly, the maturity level of all products used to develop CiPS have been upgraded from beta status to provisional or higher, meaning

Atmos. Meas. Tech. Discuss., doi:10.5194/amt-2017-64, 2017
Manuscript under review for journal Atmos. Meas. Tech.
Discussion started: 5 April 2017

Atmospheric Measurement Techniques Discussions

that the data have at least been compared to independent sources in order to correct obvious artefacts (NASA Atmospheric Science Data Center, 2010).

As described in Vaughan et al. (2009) cloud and aerosol layers are detected at three spatial resolutions: 5, 20 and 80 km. At a spatial resolution of 5 km, the signal-to-noise ratio of a faint cirrus or aerosol layer is usually too weak to be distinguished from the clear-sky atmospheric signal. By averaging 4 or 16 consecutive 5 km profiles the signal-to-noise ratio is increased, which allows for detection of very thin cirrus and aerosol layers. This can result in a vertical overlap between layers detected at different spatial resolutions. This is accounted for by identifying the part of an icy layer vertically overlapped by another layer (water cloud or aerosol) detected at a higher spatial resolution and correcting the corresponding extinction coefficients, ice water content and CTH accordingly. The column IOT and IWP are then derived by combining the cirrus properties of all icy layers in each profile. Finally, the OPF is extracted from the 'Opacity_Flag' product.

The improved quality of the V3 CALIOP products allows us to omit the filtering processes used for COCS (see Sect. 2.5). To assure a high quality dataset, the extinction quality control flag, retrieval uncertainties and the feature classification flag including the quality assessments have been considered. All columns containing at least one layer with unknown feature type, unknown cloud phase or a feature/phase quality assessment flag less than 3 (high confidence) are excluded. Additionally, only those columns with solely constrained or unconstrained retrievals where the initial lidar ratio remained unchanged during the solution process are included. Furthermore, the columns containing stratospheric features are excluded due to lack of information about whether the features are stratospheric clouds or aerosol layers.

In the following, all quantities referring to CALIOP will be denoted as IOT_{CALIOP}, IWP_{CALIOP} and CTH_{CALIOP}.

3.4 Data preparation

To learn the relationship between the SEVIRI, ECMWF, auxiliary data and the cirrus properties from CALIOP, an extensive dataset is created containing spatial and temporal collocations of all variables. The training dataset covers the time period from April 2007 to January 2013, which is the time when MSG-2 was the operational satellite at 0.0° E. CiPS is restricted to MSG-2 alone, since we did not want to mix data from multiple SEVIRI instruments since their characteristics are slightly different.

3.4.1 Data collocation

For this time period all quality controlled CALIOP data (Sect. 3.3) within the SEVIRI field of view are identified and collocated with single SEVIRI pixels in time and space. Due to the different viewing geometries of SEVIRI and CALIOP, the same cloud seen by SEVIRI and CALIOP at the same time appears to be located at two different positions. The magnitude of this displacement depends on the viewing angle and the altitude of the cloud layer. This effect has been corrected for using the latitude, longitude and cloud top altitude from CALIOP (parallax correction) to project ice clouds to the SEVIRI grid. The cirrus properties from CALIOP are spatially collocated with SEVIRI observations from the pixel having the largest overlap with the 5 km CALIOP orbit segment. The data are temporally collocated by identifying the SEVIRI observation that has the smallest difference in acquisition time compared to CALIOP. With a temporal resolution of 15 min for SEVIRI, the maximum difference in acquisition time between SEVIRI and CALIOP is 7.5 min.

Atmos. Meas. Tech. Discuss., doi:10.5194/amt-2017-64, 2017
Manuscript under review for journal Atmos. Meas. Tech.
Discussion started: 5 April 2017

The ECMWF surface temperatures are spatially collocated with the satellite observations using nearest neighbour. For the temporal collocation, the ECMWF re-analysis data are linearly interpolated between the ECMWF 6 h time steps and the satellite acquisition time.

3.4.2 Training data

The full collocated dataset, covering the entire SEVIRI disc and a time period of almost 6 years, contains close to 50 millions collocations. 80 % of those collocations are used to create the four datasets required for the training of the four ANNs contained in CiPS. For the CCF ANN, both cirrus free collocations as well as collocations with transparent and opaque cirrus clouds are included in the training dataset. Collocations with no cirrus cloud present are excluded from the training datasets used to train the OPF ANN as well as the CTH and IOT/IWP retrieval ANNs, since those networks will be applied only on pixels identified as cirrus covered by the CCF ANN. Furthermore, the IOT/IWP ANN is trained only with collocations containing transparent cirrus clouds, where the true, rather than the apparent, IOT and IWP could be retrieved by CALIOP. Figure 2 shows the relative number distributions of the CTH, IOT and IWP retrieved by CALIOP. It is clear that the collocation dataset is unbalanced in several aspects. The IOT and IWP have exponential distributions with very few thicker cirrus clouds. Similarly there are comparably few low and high cirrus clouds available and the CTH distribution has two peaks, corresponding to mid-latitudes and tropics. To improve the end performance for those rare points the unbalance of the training datasets is mildered "by hand". For the cirrus detection and IOT/IWP ANNs, four duplicates of all cirrus clouds with $\mathrm{IOT}_{\mathrm{CALIOP}} \geq 1.0$ have been added to the training datasets. Similarly four duplicates of all cirrus clouds with $\mathrm{CTH}_{\mathrm{CALIOP}} > 17\,\mathrm{km}$ or $\mathrm{CTH}_{\mathrm{CALIOP}} < 5\,\mathrm{km}$ have been added to the CTH training dataset. For the opacity classification ANN, four duplicates of all opaque cirrus clouds have been added to the training dataset. Adding too few duplicates has a negligible effect whereas too many duplicates give the added points a too strong impact during the training. By testing different numbers, four duplicates are seen to yield the best results for all ANNs. Furthermore, the IOT and IWP are transformed to their logarithmic counterparts before the training ($\mathrm{IOT}^* = \log_{10}(\mathrm{IOT}), \mathrm{IWP}^* = \log_{10}(\mathrm{IWP}/1\,\mathrm{g\,m^{-2}})$). Finally the single input variables are normalised to have zero mean and unit variance (LeCun et al., 1998) and the output data are scaled to fit the ranges of the activation functions (Sect. 2.3.1) used by the ANNs (logistic function for the classification networks and the tanh function for the regression networks).

3.4.3 Validation data

The remaining 20 % of the collocation dataset is used for validation. Half of this data is used to create internal validation datasets that are used to monitor the error against independent data during the training in order to avoid overfitting (see Sect. 3.5). The internal validation datasets have been filtered in the same manner as the training datasets, but have not been balanced by adding duplicates of selected points. The second half of the validation data is used for the final validation of CiPS (and COCS) presented in Sect. 4.2. With common ANN terminology the internal and final validation data are usually referred to as validation and test data respectively.

Atmos. Meas. Tech. Discuss., doi:10.5194/amt-2017-64, 2017
Manuscript under review for journal Atmos. Meas. Tech.
Discussion started: 5 April 2017

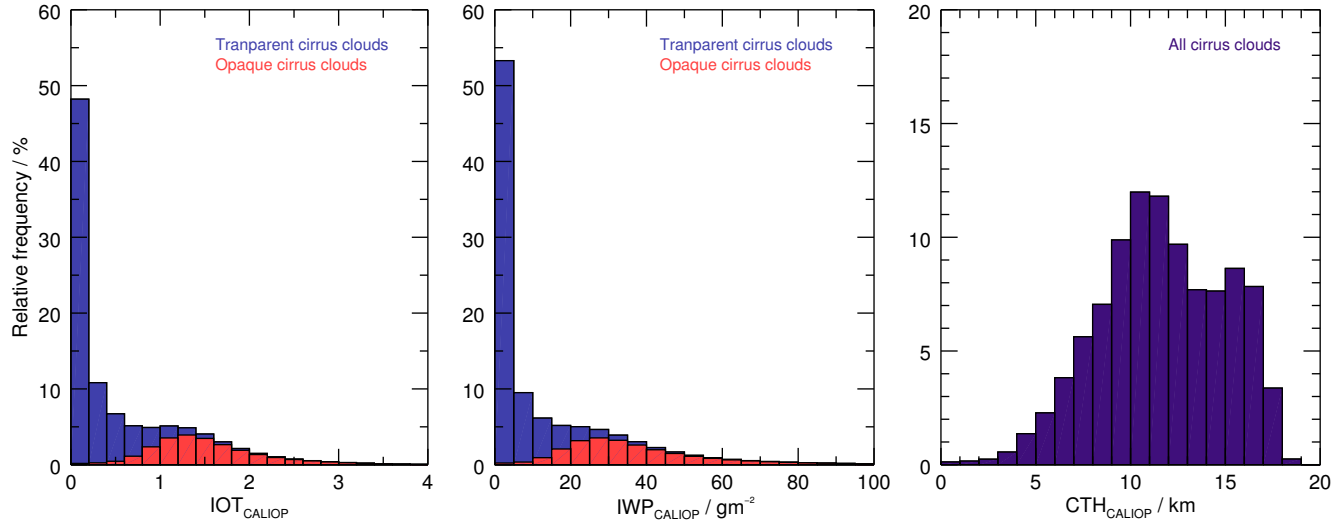

Figure 2. The relative number distribution of the cirrus IOT (bin size = 0.2), IWP (bin size = 5 gm^{-2}) and CTH (bin size = 1 km), from almost 6 years of V3 CALIOP L2 layer data over the SEVIRI disc.

3.5 Training

To train and apply CiPS the Fast Artificial Neural Network library (FANN, Nissen, 2003) is used. The four ANNs contained in CiPS are trained using the standard backpropagation algorithm described in Sect. 2.3.2 and mini-batch gradient descent.

3.5.1 Training meta-parameters

A batch size of 1024 is used, meaning that the ANNs look at 1024 input and output data combinations before each weight update. The value of 1024 was chosen as a trade-off between the noise in the error gradient that increases with smaller batch sizes and the required computational power that increases with larger batch sizes. The learning rate and momentum (Sect. 2.3.2) are sensitive to the problem that should be solved, the corresponding training data as well as the number of input and output variables (Schaul et al., 2013). To find the optimal values an extensive iterative test approach is performed. For this test a large GPU cluster (120 TFLOPs - 20 NVIDIA GTX Titan GPUs) is used to train numerous ANNs with different numbers of hidden layers and hidden neurons and a wide range of learning rates and momentum values. To find the optimal values for each meta-parameter, random search is performed within intervals chosen based on expert knowledge. All resulting optima are well within these chosen intervals, so it is assumed that the choice of the intervals does not introduce any distortion or bias. For both the classification and regression tasks a learning rate around 0.05 and momentum around 0.99 is found to provide the best performing ANNs.

Atmos. Meas. Tech. Discuss., doi:10.5194/amt-2017-64, 2017
Manuscript under review for journal Atmos. Meas. Tech.
Discussion started: 5 April 2017

3.5.2 MLP structure optimisation

The iterative tests in Sect. 3.5.1 also show that larger structures (more hidden layers and hidden neurons) are beneficial and yield lower mean square errors between the expected and estimated values. However, we want the final training of CiPS as well as the application to the 3712×3712 pixels large SEVIRI images to be manageable and computationally fast on a common standard desktop PC. Thus, for each ANN the structure is selected that offers the best trade-off between accuracy and training/application time. For each ANN contained in CiPS several networks with different structures are trained using one, two and three hidden layers with either 16 or 64 hidden neurons per hidden layer. For the single hidden layer structures we also train with 128 hidden neurons. For each structure the training is repeated twice in order to minimise the risk of having a bad end performance as a result of a bad set of initial weights (from Widrow and Nguyen's algorithm (Nguyen and Widrow, 1990)). To speed up the training, only 25 % of the respective training datasets is used at this point.

To avoid over-fitting, the error against the independent internal validation datasets (Sect. 3.4.3) is always monitored. Over-fitting occurs when an ANN learns the training dataset itself rather than the relationship between the input and output variables and thus loses its ability to generalise. To make sure that the ANNs are not over-fitting the updated weights are only saved if the error against the internal validation dataset decreases, otherwise the training continues but the set of weights having the current minimum error against the internal validation dataset is kept.

When the accuracy of the ANNs does no longer improve, the performance and speed of each structure is evaluated using the final validation data in order to find the structures that offer the best trade-off between accuracy and application time. Only the best performing network among the two that were trained for each structure is evaluated and presented here. The differences are however very small.

Figure 3a shows the POD (Eq. (3)) for the CCF ANN with respect to CALIOP for the seven different structures that were investigated. For a fair comparison the cirrus detection thresholds for the respective structures were chosen such that the average FAR (Eq. (4)) is the same for all structures, and corresponds to the FAR of the final CCF ANN in CiPS (Sect. 3.6). The MAPE (Eq. (6)) for the CTH and IOT retrieval with respect to CALIOP is shown in Fig. 3b and 3c respectively. The MAPE behaviour of the IWP is very similar to the MAPE of the IOT and is therefore not presented here. For the cirrus detection and IOT retrieval, only the transparent cirrus clouds are considered. Please note that for a better visualisation for the lower IOT values, the horizontal axes in Fig. 3a and 3c are divided into one logarithmic range ($IOT_{CALIOP} < 1.0$) and one linear range ($IOT_{CALIOP} \geq 1.0$).

Furthermore, Table 3 lists the approximate amount of time required to process 1 million data points/pixels (including I/O) on a common standard desktop PC (1 CPU à 3.40 GHz) using the different structures.

In all cases, already small networks produce reasonable results. In many cases differences between structures are not very large. Nevertheless, we also see that larger ANNs can always solve the problems in a more accurate way and especially for the cirrus cloud detection it is beneficial to either use more hidden neurons or add more hidden layers rather than using a simple structure with one hidden layer and 16 hidden neurons (denoted as 1-16). Three hidden layers with 64 neurons each (3-64) offers the highest accuracy for all cases, but processes the data significantly slower by a factor 8 or 6 compared to the smaller

Atmos. Meas. Tech. Discuss., doi:10.5194/amt-2017-64, 2017
Manuscript under review for journal Atmos. Meas. Tech.
Discussion started: 5 April 2017

Atmospheric Measurement Techniques Discussions

Table 3. Approximate time required to process 1 million data points using the different ANN structures investigated in this study. The number to the left of the hyphen is the number of hidden layers and the number to the right the number of hidden neurons per hidden layer.

Structure	1-16	2-16	3-16	1-64	1-128	2-64	3-64
Time / s	2.0	2.8	3.9	5.0	9.3	14.4	23.3

structures with 2 or 3 hidden layers and 16 neurons per layer. For the IOT retrieval, a larger ANN is only beneficial for the lower values and the MAPE seems to be saturated and not improvable for $\mathrm{IOT}_{\mathrm{CALIOP}} > 0.1$ using this approach and training data. The same is observed for the CTH for the lower clouds.

For the retrieval of CTH and IOT/IWP the ANN structures with 2 hidden layers and 16 hidden neurons (2-16) are chosen as those are considered to offer the best trade-off between accuracy and processing time. For the CCF, the structure with 3 hidden layers and 16 hidden neurons (3-16) is chosen for the same reason. For the OPF, the structure of the network does not seem to have any significant influence on the performance and is thus not presented here. The fastest structure with one hidden layer and 16 hidden neurons (1-16) is chosen for this task.

3.5.3 Optimal MLP tuning

When the four optimal ANNs have been selected, the training of the respective ANNs continues. During this final stage of the training, which we call the tuning, the batch size and the amount of training data gradually increases whereas the learning rate and momentum gradually decreases. During the first phase of the training as described in Sect. 3.5.2, a rough estimate of the error gradient is sufficient as we are interested in the direction towards a minimum solution. Thus a larger learning rate and smaller mini-batches are preferred. When the ANN approaches the region of an optimal solution, those large step-sizes and small mini-batches are too blunt to find the finer structures needed to solve the problem better. Thus the learning rate and batch size should be adjusted accordingly in order to make smaller and more informed steps in the search space. The learning rate is reduced by a factor 2 and the batch size is increased by a factor 2 at this point. In order to not impede the effect of the finer learning rate and batch size, the momentum is reduced accordingly. Furthermore the size of the training dataset, which started at 25 % during the first stage, is increased by a factor 2. The meta-parameters of the training algorithm are updated following a schedule procedure that is commonly used in the Machine Learning/ANN community. The tuning is an iterative process and the meta-parameters are refined when the total error stops to decrease. This continues until all ANNs have reached a point where additional epochs do not reduce the error, using 100 % of the respective training datasets.

Reduced errors against the reference data are observed in nearly all aspects after the tuning. The effects are however comparably small, meaning that already after the first stage where the optimal structures were sought, meaningful results were achieved (see Fig. 3).

Using the above specified desktop PC, the final set of ANNs, which we call CiPS (Cirrus Properties from SEVIRI), takes approx. 60 seconds to process a complete SEVIRI image (3712×3712 pixels) including I/O. Ca. 40 seconds are needed for the cirrus cloud detection and another 20-30 seconds for the opacity classification as well as the retrieval of CTH, IOT and IWP.

Atmos. Meas. Tech. Discuss., doi:10.5194/amt-2017-64, 2017
Manuscript under review for journal Atmos. Meas. Tech.
Discussion started: 5 April 2017

Atmospheric Measurement Techniques Discussions

The cirrus cloud detection takes longer as this ANN is applied to all SEVIRI pixels, whereas the other ANNs are only applied on those pixels classified as icy by CiPS. This is ca. 10 times faster than the combined CTH and IOT retrieval by COCS (Kox et al., 2014).

3.6 Cirrus detection and opacity classification thresholds

As described in Sect. 3.1 the thresholds for the CiPS CCF and OPF ANNs can be selected between 0–1 depending on the application. These two thresholds are chosen based on a trade-off between the POD (Eq. (3)) and FAR (Eq. (4)). It is clear that the two quantities are anti-correlated where a lower threshold yields a higher POD, but comes at the expense of an increased FAR and vice versa. For the application and validation presented in Sect. 4 and 5 as well as for the standard usage of CiPS, a CCF threshold of 0.62 is chosen, resulting in a total POD of 71 % and a FAR of 3.9 %. The low POD is a direct effect of the large amount of very thin to sub-visual cirrus (IOT< 0.03) that CiPS does not detect (see Fig. 2 and 6). For the OPF a threshold of 0.86 is chosen, resulting in a POD of 71 % and a FAR of 4.0 % for the cirrus clouds that CiPS successfully detects.

For both the CCF and OPF the POD and FAR vary smoothly with an increasing classification threshold, meaning that no evident jumps in POD and/or FAR are observed.

4 CiPS application and validation

4.1 Application

In this section CiPS is applied to the June 1, 2015 12.30 UTC SEVIRI image subset consisting of 350×350 pixels comprising western/central Europe. Figure 4a shows a false colour RGB composite that uses three SEVIRI channels centred at 0.6, 0.8 and 10.8 µm. With this channel combination the thick and thin cirrus clouds are identified as white and blueish respectively, whereas the liquid water clouds are recognised as yellow. Quite intuitively surface water and land appear as dark blue and green respectively. Two large cirrus clouds can be seen ranging from the south-western parts of France towards the Alps and southern parts of Scandinavia respectively. Also over England and Norway, cirrus clouds are present and clearly visible in the RGB. Liquid water clouds are mainly present over the central parts of France, Switzerland and Germany, but also over the North Sea, Mediterranean Sea and southern parts of Scandinavia. For an enhanced view of thin cirrus clouds Fig. 4b shows the brightness temperatures difference between the SEVIRI channels centred at 8.7 µm and 10.8 µm. In this picture, cirrus clouds are characterised by positive or slightly negative values.

Figure 4c shows the cirrus cloud mask retrieved by CiPS for the same scene. The blue and grey areas show all pixels that CiPS classify as cirrus, of which the grey pixels are classified as opaque. This means that for the grey pixels the retrieved IOT and IWP is more likely to be underestimated. CiPS clearly detects all cirrus clouds that can be identified in the false colour RGB composite (Fig. 4a) and from the brightness temperature differences (Fig. 4b). The OPF correlates well with the cirrus brightness in the RGB. The brightest parts of the cirrus clouds, which represent the thickest parts, are classified as opaque by CiPS.

Atmos. Meas. Tech. Discuss., doi:10.5194/amt-2017-64, 2017
Manuscript under review for journal Atmos. Meas. Tech.
Discussion started: 5 April 2017

Atmospheric Measurement Techniques Discussions

Figures 4d-f show the corresponding CTH, IOT and IWP retrieved by CiPS. CiPS captures the latitude dependency of the CTH, with generally lower values at higher latitudes. We also see elevated heights for the thicker cirrus cloud areas. The cloud edges are generally seen to have lower altitudes, which could indicate ice crystal sedimentation or partial cloud cover inside the SEVIRI pixels. As expected, the IOT and IWP are well correlated and qualitatively the values corresponds well to the level of transparency of the different cirrus clouds seen in Fig. 4a. For a quantitative evaluation of the IOT and IWP as well as the other quantities, readers are referred to Sect. 4.2.

4.2 Validation against CALIOP

In this section the performance of CiPS is validated against V3 CALIOP products using the 10 % subset (approx. 4.9 millions collocations) of the full collocation dataset excluded from the training of CiPS (Sect. 3.4.3). The results are presented for the full SEVIRI field of view. Since CiPS and COCS share the concept of using ANNs trained with primarily SEVIRI and CALIOP data, we also present the corresponding validation results of COCS. This clarifies the improvements of CiPS compared to COCS.

4.2.1 Cirrus classification

The CCF of CiPS and COCS and the OPF of CiPS are evaluated as a function of the geographic position. This aspect is interesting due to the very different meteorological conditions present on the SEVIRI disc. Figure 5a and 5b shows the gridded FAR (Eq. (4)) for the CCF of CiPS and COCS respectively over 5°×5° boxes, using the V3 CALIOP products as reference.

As mentioned in Sect. 3.6 the average FAR for the CiPS cirrus detection is 3.9 %. The FAR is sensitive to the frequency of the events, meaning that over regions where the natural probability of cirrus presence is high, a single false alarm will have a larger impact on the total FAR than over regions where the natural probability of cirrus presence is low. Although the FAR of CiPS is relatively homogeneous across the SEVIRI disc, this effect can be observed with higher FARs along the ITCZ and lower FARs over the Sahara desert for example.

COCS has an equally low FAR over arid regions, but has a clearly higher FAR in general. In particular over icy surfaces like Greenland and Antarctica, COCS overestimates the cirrus presence, with FARs up to approx. 90 %. But for high latitudes in general, the FAR of COCS remains higher than CiPS. In the polar regions (latitude $\geq 65°$ N/S) the average FAR is 33 % for COCS and 5.3 % for CiPS. Also over Europe the FAR of CiPS is clearly lower. Furthermore, COCS strongly overestimates the cirrus presence around the sub-satellite point of SEVIRI. For viewing zenith angles smaller than 15°, COCS has an average FAR of 23 %. This deficiency is not shown by CiPS, which has an average FAR of 8.5 % for the same area. Furthermore, a false alarm of COCS has $\text{IOT}_{\text{COCS}} \geq 0.1$, whereas a false alarm of CiPS can have an IOT_{CiPS} down to 0.0, i.e. $\text{IOT}_{\text{CiPS}} > 0.0$.

Due to the high probability of cirrus cloud presence along the ITCZ, the effect of the higher FAR of CiPS over this region is small, since a high cirrus probability prevents false alarms from occurring. Figure 5c and 5d show the total number of false alarms/positives N_{FP} by CiPS and COCS respectively, i.e. the total number of cirrus free points in the validation dataset (approx. 3.3 millions) that are falsely classified as cirrus. Again the numbers are calculated over 5°×5° boxes. Even if the probability of having a false alarm by CiPS is higher than the average FAR along the ITCZ (Fig. 5a), the absolute number of

Atmos. Meas. Tech. Discuss., doi:10.5194/amt-2017-64, 2017
Manuscript under review for journal Atmos. Meas. Tech.
Discussion started: 5 April 2017

Atmospheric Measurement Techniques Discussions

false alarms is just as high as for most regions across the SEVIRI disc (Fig. 5c). Looking at N_{FP} by COCS (Fig. 5d), more false alarms are observed at high latitudes (especially over icy surfaces), over Europe and around the sub-satellite point.

The FAR can easily be optimised by reducing the number of detected cirrus clouds. Thus it is necessary to simultaneously look at the performance in cirrus detection along side the false alarm analysis. A reduced POD (probability of detection) would be a natural effect if the FAR is reduced, but despite the low FAR of CiPS the POD remains high. Fig. 6 shows the POD of CiPS, again in comparison to COCS. The POD is a function of $\mathrm{IOT_{CALIOP}}$ and within each $\mathrm{IOT_{CALIOP}}$ interval the POD given by Eq. (3) is calculated, using the V3 CALIOP products as reference. For a better visualisation the POD is presented with a logarithmic scale for $\mathrm{IOT_{CALIOP}} < 1.0$ and with a linear scale for $\mathrm{IOT_{CALIOP}} \geq 1.0$. For cirrus clouds with $\mathrm{IOT_{CALIOP}} > 1.0$, CiPS and COCS perform similarly. A strong difference is instead seen for the thin cirrus clouds, where CiPS detects more cirrus clouds compared to COCS. For example at $\mathrm{IOT_{CALIOP}} = 0.1$, CiPS detects 71 % of the cirrus clouds and COCS 43 %. A higher POD for thin cirrus clouds is an important improvement when studying contrail cirrus or the cirrus life cycle for example. Figure 6 does only present the results for the transparent cirrus clouds where the CALIOP laser was not saturated. For the opaque cirrus clouds the average POD is 98 % for both CiPS and COCS. The geographical dependency of POD is clearly anti-correlated with the geographical dependency of the FAR, meaning that CiPS has its highest and lowest POD over regions where the natural probability of cirrus presence is high and low respectively. Apart from that, the POD of CiPS is homogeneous across the SEVIRI disc.

Fig. 7 shows the FAR of the CiPS OPF, again over 5°×5° boxes, using the V3 CALIOP products as reference. Since the OPF is a new variable introduced with CiPS, the results cannot be compared to COCS. As mentioned in Sect. 3.6 the average POD and FAR is 71 % and 4.0 % respectively. Both quantities are relatively homogeneous across the SEVIRI disc, but the risk of falsely classifying a transparent cirrus cloud as opaque is slightly lower in the tropical regions (latitude < 30° N/S).

4.2.2 Cirrus properties

Figure 8 shows two density scatter plots, with $\mathrm{CTH_{CALIOP}}$ on the vertical axes and $\mathrm{CTH_{CiPS}}$ (left) and $\mathrm{CTH_{COCS}}$ (right) on the horizontal axes. The color shows the normalised relative frequency, which is the relative frequency normalised to the interval 0–1. Along with the scatter plots the MPE and MAPE (Eq. (5) and 6) of CiPS and COCS with respect to CALIOP as a function of $\mathrm{CTH_{CALIOP}}$ is shown (right). CiPS and COCS are validated using their own respective cirrus flags, meaning that the $\mathrm{CTH_{CiPS}}$ is validated using the cirrus covered points that CiPS detects, whereas the $\mathrm{CTH_{COCS}}$ is validated using those cirrus covered points that COCS detects. Using a common cirrus flag (i.e. those cirrus covered points that both CiPS and COCS detect) shows marginal differences, with slightly reduced errors for CiPS, as a result of the reduced amount of very thin cirrus that only CiPS detect, for which the CTH is more difficult to accurately estimate.

With CiPS the CTH is retrieved with a higher accuracy compared to COCS, especially for high and low cirrus clouds. The correlation between CALIOP and CiPS is 0.90. For CALIOP and COCS, the correlation coefficient is 0.82.

The MPE shows that CiPS overestimates and underestimates the CTH of the lowest and highest cirrus clouds respectively, even if the errors are smaller than for COCS. From 8-15 km the MPE is close to zero, meaning that the CTH retrieval by CiPS is unbiased in this $\mathrm{CTH_{CALIOP}}$ range. The MAPE shows that the average magnitude of the CiPS error is 10 % or less for

Atmos. Meas. Tech. Discuss., doi:10.5194/amt-2017-64, 2017
Manuscript under review for journal Atmos. Meas. Tech.
Discussion started: 5 April 2017

Atmospheric Measurement Techniques Discussions

cirrus clouds having a CTH above 8 km. Furthermore, the MAPE clearly shows the better accuracy of CiPS. For example for cirrus clouds with a CTH_{CALIOP} between 4–5 km, representing mid-level clouds with icy tops, the MAPE is 38 % for CiPS. For COCS the corresponding number is 107 % with solely overestimated values (MAPE=MPE). This is mainly an effect of the CTH filtering used for COCS (Sect. 2.5), which excluded cirrus clouds with a $CTH_{CALIOP} < 4.5$ km from the training dataset, leading to strong overestimations of lower values.

The larger errors observed for low clouds can be attributed to the smaller temperature contrast with respect to the surface temperature and thus the weaker signal that those clouds have compared to higher cirrus clouds. Another source of error that applies to all top heights is the different sensitivities of CALIOP and SEVIRI.

The CTH has a strong latitude dependency and the CiPS results shown in Fig. 8 are not representative for all latitudes. Figure 9 shows the MPE of the CTH_{CiPS} retrievals with respect to CALIOP as a function of CTH_{CALIOP} and the latitude. The MPE shows a clear latitude dependency and in contrast to Fig. 8c, where CiPS is shown to have no bias (MPE≈0) between 8–15 km, we see that the CTH_{CALIOP} limit when CiPS starts to over- and underestimate the CTH increases towards the equator. At higher latitudes (e.g. over Europe), we see that CiPS is more likely to underestimate the CTH also for lower CTH_{CALIOP} around 10-14 km, with an increasing error towards higher latitudes. Similarly the CTH_{CiPS} for cirrus clouds with CTH_{CALIOP} <14 km is more likely to be overestimated along the ITCZ, with increasing errors towards the equator. We see a path of low bias (MPE≈0) across the latitude range which represents the areas of most occurrences, as this is the result obtained when averaging the MPE across all latitudes (8c), indicating that the situations with higher errors and stronger biases are comparably rare.

Figure 10 shows again two density scatter plots, now with IOT_{CALIOP} on the vertical axes and IOT_{CiPS} (left) and IOT_{COCS} (centre) on the horizontal axes. As before the color shows the normalised relative frequency. Again the MPE and MAPE (Eq. (5) and (6)) of CiPS and COCS with respect to CALIOP as a function of IOT_{CALIOP} is shown in the right panel. Only transparent cirrus clouds, where CALIOP was not saturated, are included here. The two algorithms are validated using their respective cirrus cloud flags (as explained above for the CTH). This is not 100 % true for the IOT_{COCS} scatter plot however, where all points with a retrieved $IOT_{COCS} > 0.0$ are included. Instead the black grid on top of the scatter plot illustrates the area where COCS does not detect any cirrus clouds as a results of the COCS cirrus detection threshold at $IOT_{COCS} = 0.1$ (Sect. 2.5). A relatively large scatter is observed for both algorithms. CiPS shows a better correlation with the CALIOP retrievals though. The correlation between CiPS and CALIOP is 0.65, whereas the correlation between COCS and CALIOP is 0.61. Furthermore, CiPS shows higher frequencies along the 1-1 line down to $IOT_{CALIOP} \approx 0.09$, but also below this value the correlation between CALIOP and CiPS is evident. Only below $IOT_{CALIOP} = 0.04$ the correlation gets lost.

For a better visualisation of the lower IOT range, where most points are located, the density scatter plots have logarithmic axes. This does however visually reduce the errors, so for a quantitative evaluation attention should be paid to the right panel in Fig. 10 showing the MPE and MAPE of CiPS and COCS with respect to CALIOP. The MPE and MAPE are functions of IOT_{CALIOP} and again the results are presented using a logarithmic scale for $IOT_{CALIOP} < 1.0$ and a linear scale for $IOT_{CALIOP} \geq 1.0$. From the MAPE the low accuracy of CiPS for sub-visual cirrus clouds becomes evident. For $IOT_{CALIOP} < 0.03$, we also see that MAPE = MPE, meaning that CiPS entirely overestimates the IOT in this region. For COCS, the same is observed for $IOT_{CALIOP} < 0.1$ as a direct effect of the inability of COCS to detect cirrus clouds with an $IOT_{COCS} < 0.1$. The opposite is

Atmos. Meas. Tech. Discuss., doi:10.5194/amt-2017-64, 2017
Manuscript under review for journal Atmos. Meas. Tech.
Discussion started: 5 April 2017

Atmospheric Measurement Techniques Discussions

observed for thicker cirrus clouds ($\mathrm{IOT_{CALIOP}} \gtrsim 2.0$), where both CiPS and COCS entirely underestimate the IOT (MAPE $=$ $-$MPE). With CiPS the IOT can be retrieved with a MAPE of 50 % or less for cirrus clouds with $0.35 \lesssim \mathrm{IOT_{CALIOP}} \lesssim 1.8$. Similarly the MAPE of the retrieved $\mathrm{IOT_{CiPS}}$ is 100 % or less for cirrus clouds with $\mathrm{IOT_{CALIOP}} > 0.07$ and 230 % or less down to sub-visual cirrus clouds ($\mathrm{IOT_{CALIOP}} > 0.03$). The corresponding MAPE for the IOT retrieved by COCS within the same $\mathrm{IOT_{CALIOP}}$ intervals are 59, 290 and 720 %. A MAPE of 100 % might seems high, but one should keep in mind that this translates into small absolute errors for such thin cirrus clouds.

The systematic under- and overestimation of extreme values by both CiPS and COCS can be attributed to the ANNs themselves. It is caused by their property to output a conservative mean value in situations with high uncertainty. In a difficult situation a conservative mean value can be understood as an average over the most likely solutions, weighted by their probability. A high uncertainty means a high variance within the distribution over these solutions. Obviously, these distributions cannot be centred around the extreme values. Thus, high uncertainty always leads to a neural network output lower than the maximum value and higher than the minimum value, respectively. This is an intrinsic effect of convex cost functions (in this case the mean squared error). A direct effect of this is the increasing errors toward the extreme values observed in Fig. 10. A similar pattern is observed, although not as strong, for the CTH retrieval by CiPS and COCS in Fig. 8.

Decreasing signal from the cirrus cloud sensitive brightness temperature differences from the SEVIRI window channels, which peak around IOT $= 2$ (Krebs et al., 2007), is another source of increasing errors toward high and low $\mathrm{IOT_{CALIOP}}$. Partial cloud cover, where the CALIOP retrieval does not represent the total radiance from the corresponding SEVIRI pixel, does also introduce a bias and underestimated $\mathrm{IOT_{CiPS}}$ with respect to CALIOP. For the lower $\mathrm{IOT_{CALIOP}}$ range, a similar scatter is observed between $\mathrm{IOT_{CALIOP}}$ and modelled IOT from IR radiances for thin cirrus clouds in Holz et al. (2016). They also show that the $\mathrm{IOT_{CALIOP}}$ bias increases with optical thickness, which would make the learning by CiPS (and COCS) more difficult for those thicker clouds.

Figure 11 shows the density scatter plot with $\mathrm{IWP_{CALIOP}}$ on the vertical axis and $\mathrm{IWP_{CiPS}}$ on the horizontal axis (left) together with the MPE and MAPE (Eq. (5) and (6)) of CiPS with respect to CALIOP as a function of $\mathrm{IWP_{CALIOP}}$ (right). Please note that again the density scatter plots have logarithmic axes and the errors are presented using logarithmic scale for the thinner cirrus clouds ($\mathrm{IWP_{CALIOP}} < 10.0$) and with linear scale for the thicker ones ($\mathrm{IWP_{CALIOP}} \geq 10.0$). Since the IWP is not retrieved by COCS, no additional results are shown here for comparison. Again only transparent cirrus clouds are included.

The scatter between $\mathrm{IWP_{CiPS}}$ and $\mathrm{IWP_{CALIOP}}$ is very similar to the one between $\mathrm{IOT_{CiPS}}$ and $\mathrm{IOT_{CALIOP}}$. This is not surprising since the IWC from CALIOP is retrieved from the measured extinction coefficients using a parametrisation. The correlation between CiPS and CALIOP is however slightly lower for the IWP retrieval (0.59) compared to the IOT retrieval. This is also expected since possible deficiencies in the CALIOP IWC parametrisation will make it more difficult for the ANN to learn the relationship between the input data and the IWP. Nevertheless, these results show that the ANN is capable of reproducing this relationship in a good way. With CiPS the IWP can be retrieved with a MAPE of 100 % or less for cirrus clouds with $\mathrm{IWP_{CALIOP}} > 1.7\,\mathrm{gm^{-2}}$ and 200 % or less down to $\mathrm{IWP_{CALIOP}} \approx 0.7\,\mathrm{gm^{-2}}$. Please notice that deviations of 100 % are common even when microwave information is considered (e.g. Holl et al., 2014, , even if their error measure is different from ours).

Again, we observe systematic under- and overestimations and increasing errors toward the extreme values. As the IWP is parametrised from the CALIOP extinction coefficients, the discussion above, about the sources of error for the IOT retrieval, applies to the IWP retrieval as well.

In contrast to the CTH retrieval, CiPS shows a stable performance for the IOT and IWP retrievals across all latitudes. The only anomaly observed is that the CiPS retrieval errors for thin to sub-visual cirrus are lower over convergence zones like the ITCZ, where they are mostly found (Sassen et al., 2009; Martins et al., 2011).

5 The cirrus life cycle with CiPS

In this section the potential of CiPS is illustrated by analysing the temporal evolution of a thin cirrus cloud throughout its life cycle. The life cycle of natural cirrus and contrails is an important aspect to study (Szantai et al., 2001; Luo and Rossow, 2004; Vazquez-Navarro et al., 2015), since knowledge about the physical processes that govern their life cycle is essential for an accurate representation in weather and climate models.

On September 26, 2014 an orographic cirrus cloud was observed south of the Alps (see Fig. 12a). Here we analyse the life cycle of an outflowing cirrus originating from this orographic cirrus. The cirrus cloud was identified south of the Pyrenees on September 26.09.2014 at 10.00 UTC from SEVIRI. A false color RGB for this scene including the contour of the CiPS cirrus mask is shown in Fig. 12a. Using the binary cirrus cloud masks obtained with CiPS and 2D image correlation the detected cirrus cloud is tracked backward and forward in time using the rapid scanning service of SEVIRI with a temporal resolution of 5 min. The minimum bounding box enclosing the selected cirrus cloud is cross-correlated with the previous/next cirrus cloud mask in order to find the position of the cirrus cloud 5 min earlier/later. The scene having the highest correlation with this bounding box is identified. A cirrus cloud patch within this scene is considered part of the tracked cirrus if it is completely or partly covered by the tracked cirrus from the previous scene. This allows for a simultaneous tracking of multiple cirrus clouds in the likely event of the tracked cirrus cloud breaking up into multiple smaller cloud patches (Fig. 12b). All cirrus clouds smaller than 5 SEVIRI pixels are filtered out. Using the CiPS opacity flag, it was concluded that the tracked cirrus cloud was transparent throughout the life cycle, indicating that the true, rather than apparent, IOT and IWP can be derived by CiPS.

The path and temporal evolution of the cirrus cloud with a temporal resolution of 120 min (2 h, apart from the first and the last step) is visualised in Fig 12b. The starting time is 5.25 UTC on 26.09.2014, while the plot ends at 0.55 UTC on 27.09.2014. Notice that the time axis runs from the right to the left in order to follow the cirrus cloud that moves from the East to the West. We see that the cirrus cloud formed from several small cirrus patches originating from the outflow of the orographic cirrus south of the Alps and moved westwards over the Mediterranean Sea and Spain before it attached to another larger cirrus cloud over the Atlantic Ocean. By tracking multiple cloud patches simultaneously the cirrus cloud can be monitored as a whole, even when it splits into several parts. Throughout the life cycle, a maximum number of 24 cirrus cloud patches were tracked and analysed simultaneously as one cirrus cloud.

The temporal evolution of the cloud horizontal area can be seen at full temporal resolution (5 min) in Fig. 13a. The same figure does also present the temporal evolution of the CTH, IOT and IWP retrieved by CiPS.

Atmos. Meas. Tech. Discuss., doi:10.5194/amt-2017-64, 2017
Manuscript under review for journal Atmos. Meas. Tech.
Discussion started: 5 April 2017

Atmospheric Measurement Techniques Discussions

The cirrus cloud detaches from the orographic cirrus at 05.25 UTC and starts to grow in size immediately. The IOT and IWP decrease for the first 30 min, but start to grow along with the horizontal area at around 06.00 UTC. The lower IOT and IWP quartiles grow comparably slow and the increased mean values are a result of an increased fraction of thicker pixels, which is indicated by steeper curves of the medians and upper quartiles. The cirrus grows in size, IOT and IWP for 4 h, before it reaches its maximum horizontal area of nearly 60 000 km^2 at around 10.00 UTC. During this time period the CTH increases slightly, but remains comparably stable, i.e. the effect of the Pyrenees, that are reached by the cloud at ca. 07.00 UTC, on CTH is small. At around 09.15 UTC the cloud starts to sink and ca. 1 h later the cloud starts to decrease in size, indicating that sufficiently warm temperatures have been reached, forcing the cloud to dissipate. Despite the dissipation, the average IOT and IWP continue to grow for another hour, reaching an average IOT_{CiPS} and IWP_{CiPS} of 0.23 and 4.2 gm^{-2}. This is observed because the comparably large areas of thin cirrus with low IOTs and IWPs are the first to dissipate, leading to smaller fraction of low IOTs and IWPs and thus higher mean values. This is confirmed by the lower quartiles that start to increase more strongly when the horizontal area turns downward at around 10.30 UTC.

The IOT and IWP start to decrease at around 11.30 UTC and continue to do so until 19.00 UTC, when just a few small and thin cirrus cloud patches remain with average IOT_{CiPS} of 0.07 and average IWP_{CiPS} of 1.0 gm^{-2}. For the same period we see that the cloud slowly starts to gain altitude and around 19.00 UTC the altitude is high enough for the cloud to once again start to grow in size, IOT and IWP. The IOT and IWP grows marginally, again as a results of an increasing fraction of thicker pixels (stable lower quartiles). The growth in size is more evident and the horizontal area increases from 2800 to 19 200 km^2 during the 3 h long period of growth. Finally the horizontal area, IOT and IWP are slightly reduced before the tracked cirrus cloud connects to another cirrus cloud at 00.55 UTC. This is seen in Fig. 12b and by the rapid growth in size, IOT and IWP. The CTH remains constant though, which tells us that the other cirrus cloud in fact is located at a similar altitude.

6 Conclusions

The CiPS algorithm presented in this work detects cirrus clouds and retrieves their CTH (cloud top height), IOT (ice optical thickness) and IWP (ice water path) along with an OPF (opacity flag) using SEVIRI, ECMWF and auxiliary data. CiPS utilises a set of four artificial neural networks, trained with V3 CALIOP L2 layer data as a reference. CiPS does not take advantage of the SEVIRI channels with significant solar contribution and can thus be used during both day and night. By using ANNs, the idea is to combine the high sensitivity and vertical resolution of CALIOP with the large spatial coverage and high temporal resolution of SEVIRI. Thus, the ultimate goal of CiPS is to retrieve CALIOP-like cirrus properties for the full SEVIRI disc (approx. one third of the Earth) every 15 min.

CiPS shows a good performance when validated against independent CALIOP data. CiPS detects 95 % of all cirrus clouds with an optical thickness of 1.0 and 71 % of all cirrus clouds with an optical thickness of 0.1. On average, CiPS correctly classifies 96 % of the cirrus free pixels. For cirrus clouds with $0.35 \lesssim IOT_{CALIOP} \lesssim 1.7$, the IOT can be retrieved with a MAPE of 50 % or less, relative to CALIOP. For cirrus clouds with $IOT_{CALIOP} \gtrsim 0.07$, CiPS retrieves the IOT with a MAPE of 100 % or less. For thinner clouds, where the cirrus signal in the SEVIRI channels is weak, the error increases, but is still 230 % or

Atmos. Meas. Tech. Discuss., doi:10.5194/amt-2017-64, 2017
Manuscript under review for journal Atmos. Meas. Tech.
Discussion started: 5 April 2017

Atmospheric Measurement Techniques Discussions

less for $\mathrm{IOT_{CALIOP}} \gtrsim 0.03$ (sub-visual cirrus). The IWP retrieved by CiPS has a similar performance, but a larger MAPE for the thinner clouds. This is expected since the IWP is parametrised from the CALIOP extinction coefficients, which means that deficiencies in the parametrisation will make it more difficult for CiPS to learn the relationship between the input and output variables during training. The CTH, which is directly measured by CALIOP, is also the variable that CiPS retrieves with the highest accuracy. For cirrus clouds with $\mathrm{CTH_{CALIOP}} \geq 8\,\mathrm{km}$, the MAPE is 10 % or lower. Since CALIOP is unable to penetrate thicker cirrus clouds, an additional ANN is trained to determine whether a cirrus cloud is opaque or not (as seen from CALIOP). 96 % of the transparent cirrus clouds that CiPS detects are correctly classified as transparent. Similarly, 71 % of the opaque cirrus clouds that CiPS detects are correctly classified as being opaque. This information is very important to discern thin cirrus, for which CiPS works very well, from thicker clouds whose IOT and IWP cannot be completely captured neither by CiPS nor by CALIOP.

CiPS has a better performance in all aspects with respect to COCS, another algorithm that uses ANNs for retrieving the CTH and IOT from SEVIRI using CALIOP as reference (Kox et al., 2014). Significant improvements have been made for the detection of the thinner cirrus clouds and the retrieval of the corresponding IOT. Also for the higher and lower cirrus clouds, the CTH retrieval has been clearly improved. Furthermore, IWP and an OPF have been added.

As an application example the life cycle of a thin cirrus cloud and the temporal evolution of its properties is investigated. The cirrus cloud lives for nearly 20 h and is shown to originate from outflowing cirrus cloud patches from an orographic cirrus cloud. By analysing the cirrus properties retrieved by CiPS, the physical processes throughout the cirrus life cycle can be better understood.

The approach of using ANNs is very fast and requires little computational power compared to standard physical methods that require extensive radiative transfer calculations and/or interpolation in a multi-dimensional space. On a common standard PC, one complete SEVIRI image with 3712×3712 pixels is processed in approx. 60 s including the cirrus detection and the CTH, IOT, IWP and OPF retrieval. By training multiple ANNs with different numbers of hidden layers and hidden neurons, we see that a larger network with more hidden layers and hidden neurons does generally provide a higher POD and lower errors. A larger network does however come at the expense of more computational power, especially for the training but also for the application.

With CiPS we are now able to study the temporal evolution, life cycles and diurnal cycles of thin cirrus clouds, natural and anthropogenic (contrails), including their coverage, CTH, IOT and IWP with a higher degree of accuracy. The inclusion of a physical variable like the IWP further allows for direct comparison with weather, climate or LES models.

Atmos. Meas. Tech. Discuss., doi:10.5194/amt-2017-64, 2017
Manuscript under review for journal Atmos. Meas. Tech.
Discussion started: 5 April 2017

Atmospheric Measurement Techniques Discussions

Appendix A: List of abbreviations

ANN	Artificial Neural Network
CCF	Cirrus Cloud Flag
CTH	Cloud Top Height
FAR	False Alarm Rate
IOT	Ice Optical Thickness
ITCZ	Inter-Tropical Convergence Zone
IWP	Ice Water Path
MAPE	Mean Absolute Percentage Error
MPE	Mean Percentage Error
MLP	Multi-Layer perceptron
OPF	Opacity Flag
POD	Probability of Detection

Acknowledgements. This research was supported by the DLR/DAAD Research Fellowship Programme für Doktoranden, 14.

We thank the NASA Atmospheric Science Data Center for their kind support and for providing the V3 CALIOP layer data in a subsetted form. We also thank Mark Vaughan for his guidance on how to properly account for the vertical overlap of cloud and aerosol features in the CALIOP layer products. We want to express our gratitude to Diego Loyola for an interesting and helpful discussion about the application of ANNs in satellite remote sensing. We also thank Stephan Kox for the discussion on COCS and the relevant routines that that were provided. We gratefully acknowledge the constructive comments of Florian Ewald, André Butz and Ulrich Schumann, that improved the quality of this manuscript.

The SEVIRI data were provided by EUMETSAT and the modelled surface temperature was obtained from the European Centre For Medium-Range Weather Forecasts (ECMWF).

References

Ackerman, S., Holz, R., Frey, R., Eloranta, E., Maddux, B., and McGill, M.: Cloud detection with MODIS. Part II: validation, J. Atmos. Oceanic Technol., 25, 1073–1086, 2008.

Ackerman, S. A., Smith, W. L., Revercomb, H. E., and Spinhirne, J. D.: The 27–28 October 1986 FIRE IFO Cirrus Case Study: Spectral Properties of Cirrus Clouds in the 8–12 μm Window, Mon. Wea. Rev., 118, 2377–2388, doi:10.1175/1520-0493(1990)118<2377:TOFICC>2.0.CO;2, 1990.

Ackerman, S. A., Strabala, K. I., Menzel, W. P., Frey, R. A., Moeller, C. C., and Gumley, L. E.: Discriminating clear sky from clouds with MODIS, Journal of geophysical research, 103, 32 141–32 157, 1998.

Avery, M., Winker, D., Heymsfield, A., Vaughan, M., Young, S., Hu, Y., and Trepte, C.: Cloud ice water content retrieved from the CALIOP space-based lidar, Geophys. Res. Lett., 39, 2012.

Bugliaro, L., Zinner, T., Keil, C., Mayer, B., Hollmann, R., Reuter, M., and Thomas, W.: Validation of cloud property retrievals with simulated satellite radiances: a case study for SEVIRI, Atmos. Chem. Phys., 11, 5603–5624, doi:10.5194/acp-11-5603-2011, 2011.

CALIPSO Science Team: CALIPSO/CALIOP Level 2, Lidar Aerosol Layer Data, version 3.01 and 3.02, Hampton, VA, USA: NASA Atmospheric Science Data Center (ASDC). Provided in a subsetted form by ASDC in January 2016., 2016a.

CALIPSO Science Team: CALIPSO/CALIOP Level 2, Lidar Cloud Layer Data, version 3.01 and 3.02, Hampton, VA, USA: NASA Atmospheric Science Data Center (ASDC). Provided in a subsetted form by ASDC in January 2016., 2016b.

Cerdena, A., Gonzalez, A., and Perez, J.: Neural Network based Retrieval of Cirrus Properties, in: 2006 IEEE International Symposium on Geoscience and Remote Sensing, pp. 589–592, doi:10.1109/IGARSS.2006.155, 2006.

Cerdena, A., Gonzalez, A., and Perez, J.: Remote Sensing of Water Cloud Parameters Using Neural Networks, J. Atmos. Oceanic Technol., 24, 52–63, doi:10.1175/JTECH1943.1, 2007.

Chen, T., Rossow, W. B., and Zhang, Y.: Radiative effects of cloud-type variations, J. Climate, 13, 264–286, 2000.

Dee, D. P., Uppala, S. M., Simmons, A. J., Berrisford, P., Poli, P., Kobayashi, S., Andrae, U., Balmaseda, M. A., Balsamo, G., Bauer, P., Bechtold, P., Beljaars, A. C. M., van de Berg, L., Bidlot, J., Bormann, N., Delsol, C., Dragani, R., Fuentes, M., Geer, A. J., Haimberger, L., Healy, S. B., Hersbach, H., Holm, E. V., Isaksen, L., Kållberg, P., Köhler, M., Matricardi, M., McNally, A. P., Monge-Sanz, B. M., Morcrette, J.-J., Park, B.-K., Peubey, C., de Rosnay, P., Tavolato, C., Thepaut, J.-N., and Vitart, F.: The ERA-Interim reanalysis: configuration and performance of the data assimilation system, Quart. J. Roy. Meteor. Soc., 137, 553–597, doi:10.1002/qj.828, 2011.

Derrien, M. and LeGleau, H.: MSG/SEVIRI cloud mask and type from SAFNWC, Int. J. Remote Sens., 26, 4707–4732, 2005.

Derrien, M., Farki, B., Harang, L., LeGleau, H., Noyalet, A., Pochic, D., and Sairouni, A.: Automatic cloud detection applied to NOAA-11/AVHRR imagery, Rem. Sens. Envir., 46, 246–267, 1993.

Eliasson, S., Buehler, S. A., Milz, M., Eriksson, P., and John, V. O.: Assessing observed and modelled spatial distributions of ice water path using satellite data, Atmos. Chem. Phys., 11, 375–391, 2011.

Ewald, F., Bugliaro, L., Mannstein, H., and Mayer, B.: An improved cirrus detection algorithm MeCiDA2 for SEVIRI and its evaluation with MODIS, Atmos. Meas. Tech., 6, 309–322, doi:10.5194/amt-6-309-2013, 2013.

Eyre, J. R. and Menzel, W. P.: Retrieval of Cloud Parameters from Satellite Sounder Data: A Simulation Study, J. Appl. Meteor., 28, 267–275, doi:10.1175/1520-0450(1989)028<0267:ROCPFS>2.0.CO;2, 1989.

Fu, Q. and Liou, K. N.: Parameterization of the radiative properties of cirrus clouds, J. Atmos. Sci., 50, 2008–2025, 1993.

Gao, B., Yang, P., Han, W., Li, R., and Wiscombe, W.: An algorithm using visible and 1.38-μm channels to retrieve cirrus cloud reflectances from aircraft and satellite data, IEEE Trans. Geosci. Remote Sens., 40, 1659–1668, doi:10.1109/TGRS.2002.802454, 2002.

Hamann, U., Walther, A., Baum, B., Bennartz, R., Bugliaro, L., Derrien, M., Francis, P. N., Heidinger, A., Joro, S., Kniffka, A., Le Gléau, H., Lockhoff, M., Lutz, H.-J., Meirink, J. F., Minnis, P., Palikonda, R., Roebeling, R., Thoss, A., Platnick, S., Watts, P., and Wind, G.: Remote sensing of cloud top pressure/height from SEVIRI: analysis of ten current retrieval algorithms, Atmos. Meas. Tech., 7, 2839–2867, doi:10.5194/amt-7-2839-2014, 2014.

Heidinger, A. K. and Pavolonis, M. J.: Gazing at Cirrus Clouds for 25 Years through a Split Window. Part I: Methodology, J. Appl. Meteor. Climatol., 48, 1100–1116, doi:10.1175/2008JAMC1882.1, 2009.

Heidinger, A. K., Li, Y., Baum, B. A., Holz, R. E., Platnick, S., and Yang, P.: Retrieval of cirrus cloud optical depth under day and night conditions from MODIS Collection 6 cloud property data, Remote Sens., 7, 7257–7271, 2015.

Heymsfield, A. J., Winker, D., and van Zadelhoff, G.-J.: Extinction-ice water content-effective radius algorithms for CALIPSO, Geophys. Res. Lett., 32, doi:10.1029/2005GL022742, l10807, 2005.

Hlavka, D. L., Yorks, J. E., Young, S. A., Vaughan, M. A., Kuehn, R. E., McGill, M. J., and Rodier, S. D.: Airborne validation of cirrus cloud properties derived from CALIPSO lidar measurements: Optical properties, J. Geophys. Res. Atmos., 117, 2012.

Holl, G., Eliasson, S., Mendrok, J., and Buehler, S. A.: SPARE-ICE: Synergistic ice water path from passive operational sensors, J. Geophys. Res. Atmos., 119, 1504–1523, doi:10.1002/2013JD020759, 2014.

Holz, R., Ackerman, S., Nagle, F., Frey, R., Dutcher, S., Kuehn, R., Vaughan, M., and Baum, B.: Global Moderate Resolution Imaging Spectroradiometer (MODIS) cloud detection and height evaluation using CALIOP, J. Geophys. Res. Atmos., 113, 2008.

Holz, R. E., Platnick, S., Meyer, K., Vaughan, M., Heidinger, A., Yang, P., Wind, G., Dutcher, S., Ackerman, S., Amarasinghe, N., et al.: Resolving ice cloud optical thickness biases between CALIOP and MODIS using infrared retrievals, Atmos. Chem. Phys., 16, 5075–5090, 2016.

Hu, Y., Winker, D., Vaughan, M., Lin, B., Omar, A., Trepte, C., Flittner, D., Yang, P., Nasiri, S. L., Baum, B., Holz, R., Sun, W., Liu, Z., Wang, Z., Young, S., Stamnes, K., Huang, J., and Kuehn, R.: CALIPSO/CALIOP Cloud Phase Discrimination Algorithm, J. Atmos. Oceanic Technol., 26, 2293–2309, doi:10.1175/2009JTECHA1280.1, 2009.

Inoue, T.: On the temperature and effective emissivity determination of semi-transparent cirrus clouds by bi-spectral measurements in the 10 μm window region, J. Meteor. Soc. Japan, 63, 88–99, 1985.

Jensen, E., Kinne, S., and Toon, O.: Tropical cirrus cloud radiative forcing: Sensitivity studies, Geophys. Res. Lett., 21, 2023–2026, 1994.

Kox, S., Bugliaro, L., and Ostler, A.: Retrieval of cirrus cloud optical thickness and top altitude from geostationary remote sensing, Atmos. Meas. Tech., 7, 3233–3246, doi:10.5194/amt-7-3233-2014, 2014.

Krebs, W., Mannstein, H., Bugliaro, L., and Mayer, B.: Technical note: A new day- and night-time Meteosat Second Generation Cirrus Detection Algorithm MeCiDA, Atmos. Chem. Phys., 7, 6145–6159, doi:10.5194/acp-7-6145-2007, 2007.

Kriebel, K., Gesell, G., Kästner, M., and Mannstein, H.: The cloud analysis tool APOLLO: improvements and validations, Int. J. Remote Sens., 24, 2389–2408, 2003.

LeCun, Y., Bottou, L., Orr, G., and Müller, K.: Efficient BackProp, Neural Networks: Tricks of the Trade, pp. 546–546, 1998.

Liou, K.: An introduction to atmospheric radiation, vol. 84, International geophysics series, 2 edn., 2002.

Liu, Z., Vaughan, M., Winker, D., Kittaka, C., Getzewich, B., Kuehn, R., Omar, A., Powell, K., Trepte, C., and Hostetler, C.: The CALIPSO Lidar Cloud and Aerosol Discrimination: Version 2 Algorithm and Initial Assessment of Performance, J. Atmos. Oceanic Technol., 26, 1198–1213, doi:10.1175/2009JTECHA1229.1, 2009.

Luo, Z. and Rossow, W. B.: Characterizing Tropical Cirrus Life Cycle, Evolution, and Interaction with Upper-Tropospheric Water Vapor Using Lagrangian Trajectory Analysis of Satellite Observations, J. Climate, 17, 4541–4563, doi:10.1175/3222.1, 2004.

Martins, E., Noel, V., and Chepfer, H.: Properties of cirrus and subvisible cirrus from nighttime Cloud-Aerosol Lidar with Orthogonal Polarization (CALIOP), related to atmospheric dynamics and water vapor, J. Geophys. Res. Atmos., 116, doi:10.1029/2010JD014519, d02208, 2011.

McGill, M., Hlavka, D., Hart, W., Scott, V. S., Spinhirne, J., and Schmid, B.: Cloud physics lidar: Instrument description and initial measurement results, Appl. Opt., 41, 3725–3734, 2002.

Meerkötter, R., Schumann, U., Doelling, D., Minnis, P., Nakajima, T., and Tsushima, Y.: Radiative forcing by contrails, Ann. Geophysicae, 17, 1080–1094, 1999.

Menzel, W., Smith, W., and Stewart, T.: Improved cloud motion wind vector and altitude assignment using VAS, J. Appl. Meteor., 22, 377–384, 1983.

Menzel, W. P., Frey, R. A., Zhang, H., Wylie, D. P., Moeller, C. C., Holz, R. E., Maddux, B., Baum, B. A., Strabala, K. I., and Gumley, L. E.: MODIS Global Cloud-Top Pressure and Amount Estimation: Algorithm Description and Results, J. Appl. Meteor. Climatol., 47, 1175–1198, doi:10.1175/2007JAMC1705.1, 2008.

Minnis, P., Sun-Mack, S., Young, D. F., Heck, P. W., Garber, D. P., Chen, Y., Spangenberg, D. A., Arduini, R. F., Trepte, Q. Z., Smith, W. L., Ayers, J. K., Gibson, S. C., Miller, W. F., Hong, G., Chakrapani, V., Takano, Y., Liou, K. N., Xie, Y., and Yang, P.: CERES Edition-2 Cloud Property Retrievals Using TRMM VIRS and Terra and Aqua MODIS Data—Part I: Algorithms, IEEE Trans. Geosci. Remote Sens., 49, 4374–4400, doi:10.1109/TGRS.2011.2144601, 2011.

Minnis, P., Hong, G., Sun-Mack, S., Smith, W. L., Chen, Y., and Miller, S. D.: Estimating nocturnal opaque ice cloud optical depth from MODIS multispectral infrared radiances using a neural network method, J. Geophys. Res. Atmos., 121, 4907–4932, doi:10.1002/2015JD024456, 2016.

Nakajima, T. and King, M. D.: Determination of the Optical Thickness and Effective Particle Radius of Clouds from Reflected Solar Radiation Measurements. Part I: Theory, J. Atmos. Sci., 47, 1878–1893, doi:10.1175/1520-0469(1990)047<1878:DOTOTA>2.0.CO;2, 1990.

NASA Atmospheric Science Data Center: CALIPSO Quality Statements Lidar Level 2 Cloud and Aerosol Layer Products Version Releases: 3.01, 3.02, https://eosweb.larc.nasa.gov/sites/default/files/project/calipso/q- uality_summaries/CALIOP_L2LayerProducts_3.01.pdf, 2010.

Nguyen, D. and Widrow, B.: Improving the learning speed of 2-layer neural networks by choosing initial values of the adaptive weights, in: Neural Networks, 1990., 1990 IJCNN International Joint Conference on, pp. 21–26, IEEE, 1990.

Nieman, S., Schmetz, J., and Menzel, W.: A comparison of several techniques to assign heights to cloud tracers, J. Appl. Meteor., 32, 1559–1568, 1993.

Nissen, S.: Implementation of a Fast Artificial Neural Network Library (fann), Tech. rep., Department of Computer Science University of Copenhagen (DIKU), http://fann.sf.net, 2003.

Platnick, S., King, M. D., Ackerman, S. A., Menzel, W. P., Baum, B. A., Riedi, J. C., and Frey, R. A.: The MODIS cloud products: algorithms and examples from Terra, IEEE Trans. Geosci. Remote Sens., 41, 459–473, doi:10.1109/TGRS.2002.808301, 2003.

Prabhakara, C., Fraser, R. S., Dalu, G., Wu, M.-L. C., Curran, R. J., and Styles, T.: Thin Cirrus Clouds: Seasonal Distribution over Oceans Deduced from Nimbus-4 IRIS, J. Appl. Meteor., 27, 379–399, doi:10.1175/1520-0450(1988)027<0379:TCCSDO>2.0.CO;2, 1988.

Rumelhart, D. E., Hinton, G. E., and Williams, R. J.: Parallel Distributed Processing: Explorations in the Microstructure of Cognition, Vol. 1, chap. Learning Internal Representations by Error Propagation, pp. 318–362, MIT Press, Cambridge, MA, USA, 1986.

Sassen, K., Wang, Z., and Liu, D.: Cirrus clouds and deep convection in the tropics: Insights from CALIPSO and CloudSat, J. Geophys. Res. Atmos., 114, doi:10.1029/2009JD011916, d00H06, 2009.

Saunders, R. W. and Kriebel, K. T.: An improved method for detecting clear sky and cloudy radiances from AVHRR data, Int. J. Remote Sens., 9, 123–150, 1988.

Sayer, A. M., Poulsen, C. A., Arnold, C., Campmany, E., Dean, S., Ewen, G. B. L., Grainger, R. G., Lawrence, B. N., Siddans, R., Thomas, G. E., and Watts, P. D.: Global retrieval of ATSR cloud parameters and evaluation (GRAPE): dataset assessment, Atmos. Chem. Phys., 11, 3913–3936, doi:10.5194/acp-11-3913-2011, 2011.

Schaul, T., Zhang, S., and LeCun, Y.: No more pesky learning rates, In Proceedings of the 30th International Conference on Machine Learning (ICML-13), pp. 343–351, 2013.

Schmetz, J., Holmlund, K., Hoffman, J., Strauss, B., Mason, B., Gaertner, V., Koch, A., and van de Berg, L.: Operational cloud-motion winds from Meteosat infrared images, J. Appl. Meteor., 32, 1206–1225, doi:10.1175/1520-0450(1993)032<1206:OCMWFM>2.0.CO;2, 1993.

Schmetz, J., Pili, P., Tjemkes, S., Just, D., Kerkmann, J., Rota, S., and Ratier, A.: An Introduction to Meteosat Second Generation (MSG), Bull. Amer. Meteor. Soc., 83, 977–992, doi:10.1175/1520-0477(2002)083<0977:AITMSG>2.3.CO;2, 2002.

Schmidhuber, J.: Deep learning in neural networks: An overview, Neural networks, 61, 85–117, 2015.

Smith, W. and Platt, C.: Intercomparison of radiosonde, ground-based laser, and satellite-deduced cloud heights, J. Appl. Meteor., 17, 1796–1802, 1978.

Smith, W., Woolf, H., and Jacob, W.: A regression method for obtaining real-time temperature and geopotential height profiles from satellite spectrometer measurements and its application to Nimbus-3 SIRS observations, Mon. Wea. Rev., 98, 604–611, 1970.

Stengel, M., Kniffka, A., Meirink, J. F., Lockhoff, M., Tan, J., and Hollmann, R.: CLAAS: the CM SAF cloud property data set using SEVIRI, Atmos. Chem. Phys., 14, 4297–4311, doi:10.5194/acp-14-4297-2014, 2014.

Stephens, G. L., Vane, D. G., Boain, R. J., Mace, G. G., Sassen, K., Wang, Z., Illingworth, A. J., O'Connor, E. J., Rossow, W. B., Durden, S. L., Miller, S. D., Austin, R. T., Benedetti, A., Mitrescu, C., and Team, T. C. S.: THE CLOUDSAT MISSION AND THE A-TRAIN, Bull. Amer. Meteor. Soc., 83, 1771–1790, doi:10.1175/BAMS-83-12-1771, 2002.

Stubenrauch, C. J., Cros, S., Guignard, A., and Lamquin, N.: A 6-year global cloud climatology from the Atmospheric InfraRed Sounder AIRS and a statistical analysis in synergy with CALIPSO and CloudSat, Atmos. Chem. Phys., 10, 7197–7214, doi:10.5194/acp-10-7197-2010, 2010.

Stubenrauch, C. J., Rossow, W. B., Kinne, S., Ackerman, S., Cesana, G., Chepfer, H., Girolamo, L. D., Getzewich, B., Guignard, A., Heidinger, A., Maddux, B. C., Menzel, W. P., Minnis, P., Pearl, C., Platnick, S., Poulsen, C., Riedi, J., Sun-Mack, S., Walther, A., Winker, D., Zeng, S., and Zhao, G.: Assessment of Global Cloud Datasets from Satellites: Project and Database Initiated by the GEWEX Radiation Panel, Bull. Amer. Meteor. Soc., 94, 1031–1049, doi:10.1175/BAMS-D-12-00117.1, 2013.

Szantai, A., Désalmand, F., and Desbois, M.: Monitoring the life cycle of cirrus clouds using Meteosat-4 data during ICE-1989, Meteor. Appl., 8, 153–168, doi:10.1017/S1350482701002031, 2001.

Szejwach, G.: Determination of semi-transparent cirrus cloud temperatures from infrared radiances: Application to Meteosat, J. Appl. Meteor., 21, 384–393, 1982.

Taravat, A., Proud, S., Peronaci, S., Del Frate, F., and Oppelt, N.: Multilayer Perceptron Neural Networks Model for Meteosat Second Generation SEVIRI Daytime Cloud Masking, Remote Sens., 7, 1529–1539, 2015.

Vaughan, M. A., Powell, K. A., Winker, D. M., Hostetler, C. A., Kuehn, R. E., Hunt, W. H., Getzewich, B. J., Young, S. A., Liu, Z., and McGill, M. J.: Fully Automated Detection of Cloud and Aerosol Layers in the CALIPSO Lidar Measurements, J. Atmos. Oceanic Technol., 26, 2034–2050, doi:10.1175/2009JTECHA1228.1, 2009.

Vazquez-Navarro, M., Mannstein, H., and Kox, S.: Contrail life cycle and properties from 1 year of MSG/SEVIRI rapid-scan images, Atmos. Chem. Phys., 15, 8739–8749, 2015.

Waliser, D. E., Li, J.-L. F., Woods, C. P., Austin, R. T., Bacmeister, J., Chern, J., Del Genio, A., Jiang, J. H., Kuang, Z., Meng, H., Minnis, P., Platnick, S., Rossow, W. B., Stephens, G. L., Sun-Mack, S., Tao, W.-K., Tompkins, A. M., Vane, D. G., Walker, C., and Wu, D.: Cloud ice: A climate model challenge with signs and expectations of progress, J. Geophys. Res. Atmos., 114, doi:10.1029/2008JD010015, d00A21, 2009.

Wang, C., Platnick, S., Zhang, Z., Meyer, K., and Yang, P.: Retrieval of ice cloud properties using an optimal estimation algorithm and MODIS infrared observations: 1. Forward model, error analysis, and information content, J. Geophys. Res. Atmos., 121, 5809–5826, doi:10.1002/2015JD024526, 2015JD024526, 2016.

Watts, P. D., Bennartz, R., and Fell, F.: Retrieval of two-layer cloud properties from multispectral observations using optimal estimation, J. Geophys. Res. Atmos., 116, doi:10.1029/2011JD015883, d16203, 2011.

Wendisch, M., Yang, P., and Pilewskie, P.: Effects of ice crystal habit on thermal infrared radiative properties and forcing of cirrus, J. Geophys. Res. Atmos., 112, 2007.

Winker, D. M., Vaughan, M. A., Omar, A., Hu, Y., Powell, K. A., Liu, Z., Hunt, W. H., and Young, S. A.: Overview of the CALIPSO Mission and CALIOP Data Processing Algorithms, J. Atmos. Oceanic Technol., 26, 2310–2323, doi:10.1175/2009JTECHA1281.1, 2009.

Yorks, J. E., Hlavka, D. L., Vaughan, M. A., McGill, M. J., Hart, W. D., Rodier, S., and Kuehn, R.: Airborne validation of cirrus cloud properties derived from CALIPSO lidar measurements: Spatial properties, J. Geophys. Res. Atmos., 116, 2011.

Young, S. A. and Vaughan, M. A.: The Retrieval of Profiles of Particulate Extinction from Cloud-Aerosol Lidar Infrared Pathfinder Satellite Observations (CALIPSO) Data: Algorithm Description, J. Atmos. Oceanic Technol., 26, 1105–1119, doi:10.1175/2008JTECHA1221.1, 2009.

Yue, Q. and Liou, K.: Cirrus cloud optical and microphysical properties determined from AIRS infrared spectra, Geophys. Res. Lett., 36, 2009.

Zhang, H. and Menzel, W. P.: Improvement in thin cirrus retrievals using an emissivity-adjusted CO2 slicing algorithm, 107, AAC 2–1–AAC 2–11, doi:10.1029/2001JD001037, 2002.

Zhang, Y., Macke, A., and Albers, F.: Effect of crystal size spectrum and crystal shape on stratiform cirrus radiative forcing, Atmos. Res., 52, 59–75, doi:10.1016/S0169-8095(99)00026-5, 1999.

Atmos. Meas. Tech. Discuss., doi:10.5194/amt-2017-64, 2017
Manuscript under review for journal Atmos. Meas. Tech.
Discussion started: 5 April 2017

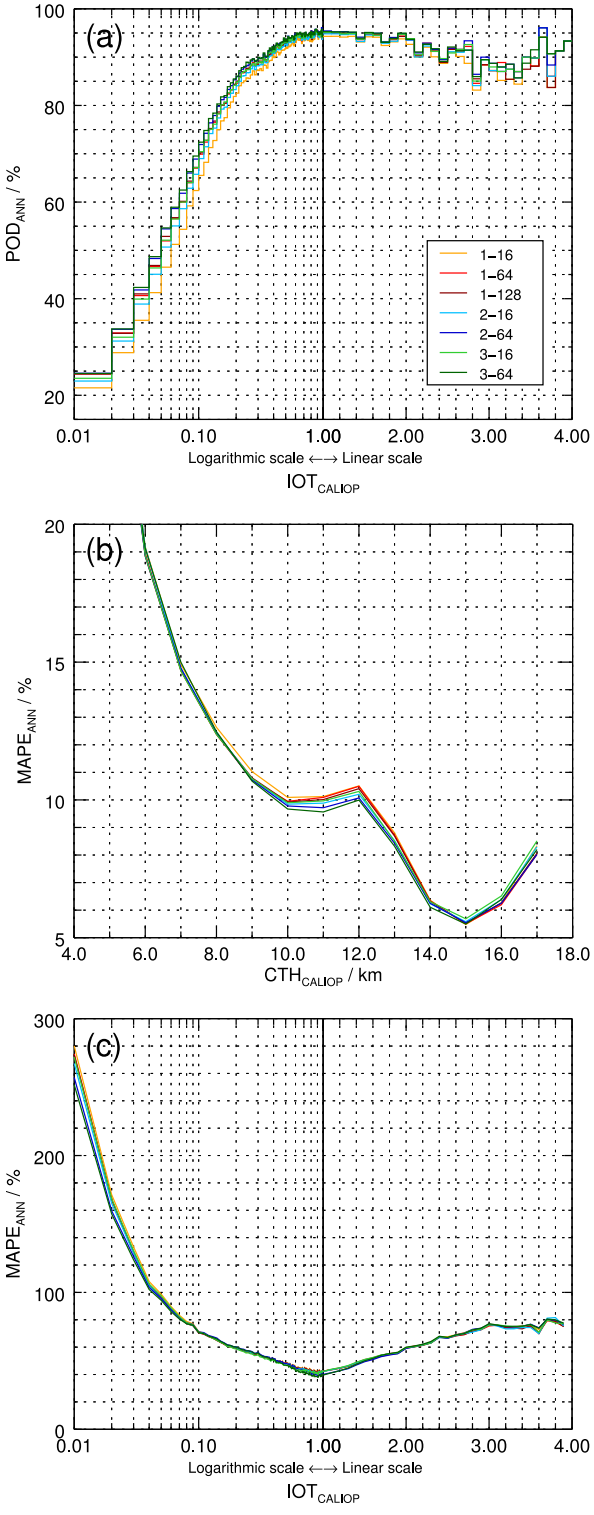

Figure 3. (a) The POD for the CiPS CCF, (b) the MAPE for the CiPS CTH retrieval and (c) the MAPE for the CiPS IOT retrieval for the different ANN structures investigated in this study. The number to the left of the hyphen is the number of hidden layers and the number to the right the number of hidden neurons per hidden layer.

Atmos. Meas. Tech. Discuss., doi:10.5194/amt-2017-64, 2017
Manuscript under review for journal Atmos. Meas. Tech.
Discussion started: 5 April 2017

Atmospheric Measurement Techniques Discussions

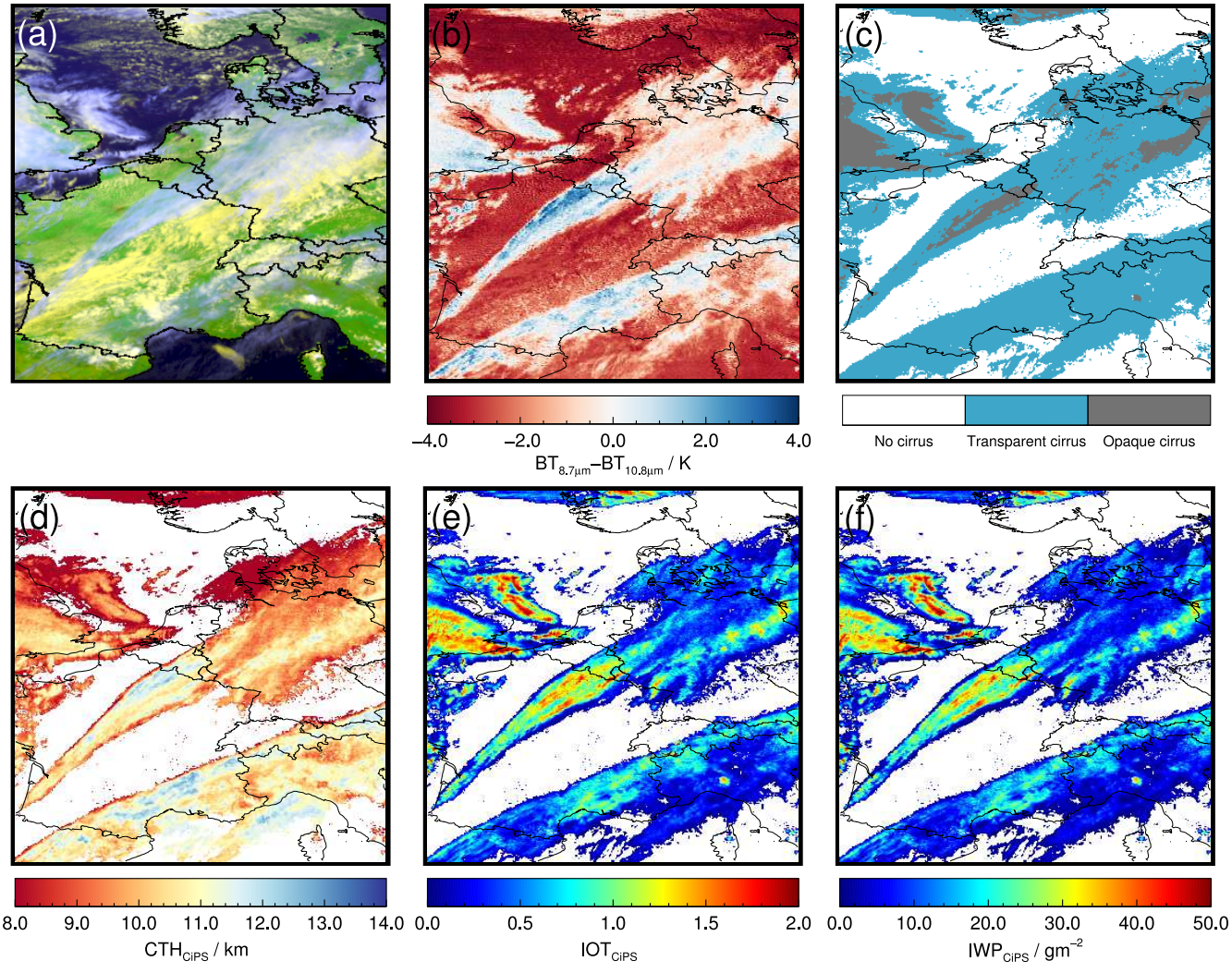

Figure 4. (a) SEVIRI false colour RGB composite over parts of Europe on June 1st, 2015 at 12.30 UTC and the corresponding (b) brightness temperature difference $BT_{8.7\mu m}$-$BT_{10.8\mu m}$ (c) cirrus cloud mask with opacity information, (d) CTH, (e) IOT and (f) IWP retrieved by CiPS.

Atmos. Meas. Tech. Discuss., doi:10.5194/amt-2017-64, 2017
Manuscript under review for journal Atmos. Meas. Tech.
Discussion started: 5 April 2017

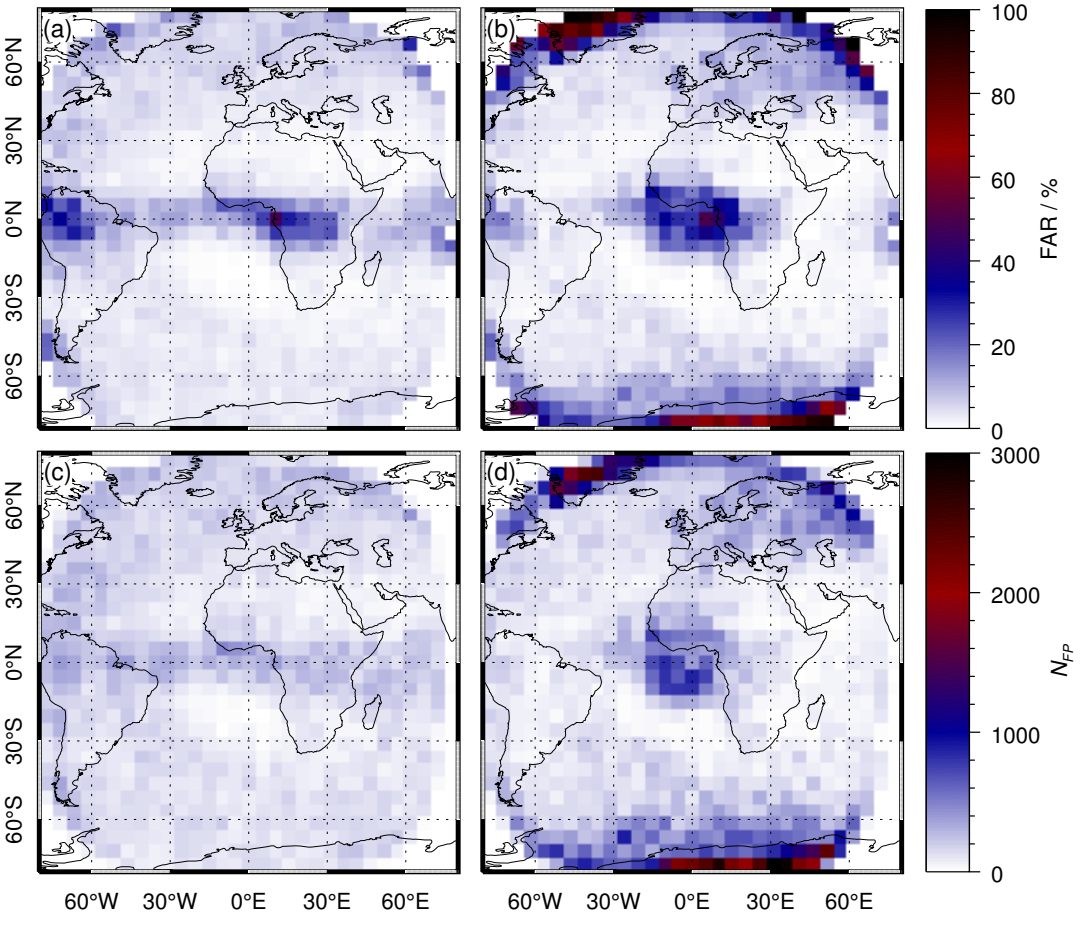

Figure 5. Top: the FAR of the CCF retrieved by CiPS (a) and COCS (b). Bottom: the absolute number of false alarms by CiPS (c) and COCS (d). Approx. 3.3 millions cirrus free points are included in the validation dataset.

Atmos. Meas. Tech. Discuss., doi:10.5194/amt-2017-64, 2017
Manuscript under review for journal Atmos. Meas. Tech.
Discussion started: 5 April 2017

Atmospheric Measurement Techniques Discussions

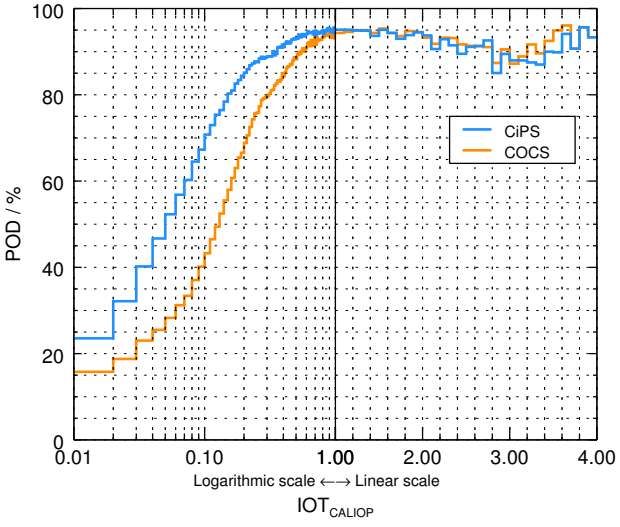

Figure 6. The POD of CiPS and COCS as a function of the IOT retrieved by CALIOP.

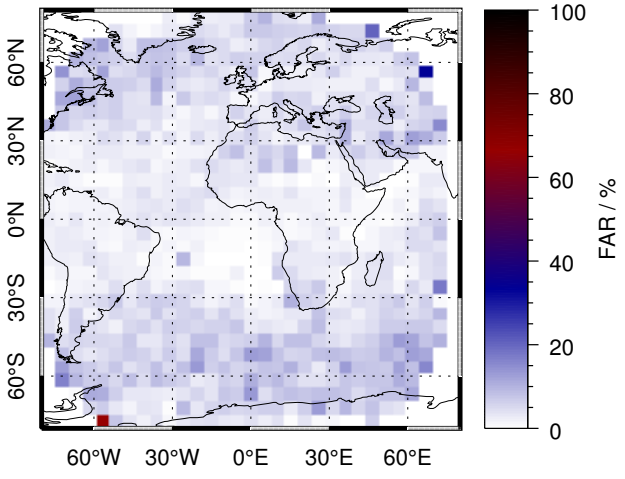

Figure 7. FAR of the CiPS OPF (opacity flag).

Atmos. Meas. Tech. Discuss., doi:10.5194/amt-2017-64, 2017
Manuscript under review for journal Atmos. Meas. Tech.
Discussion started: 5 April 2017

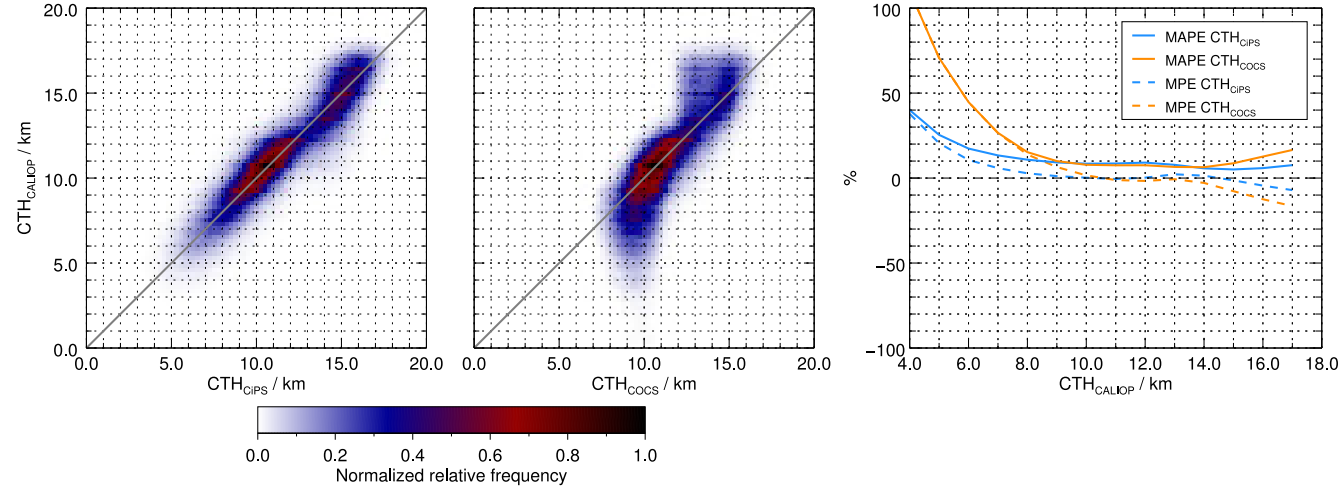

Figure 8. (Left) Density scatter plots with the CTH retrieved by CiPS and (centre) COCS on the horizontal axes and the corresponding V3 CALIOP data on the vertical axes. The grey lines represent the 1-1 line. (Right) The MAPE (solid) and MPE (dash) of the CTH retrieved by CiPS and COCS with respect to the CTH measured by CALIOP.

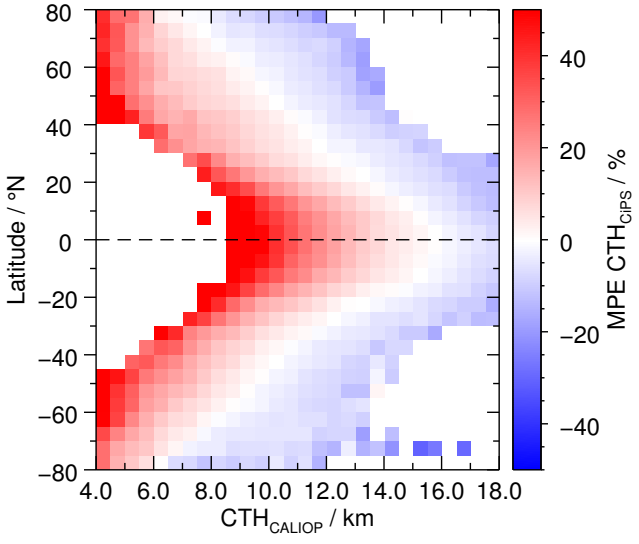

Figure 9. 2D histogram showing the MPE of the CTH_{CiPS} retrieval as a function of the reference CTH retrieval by CALIOP and the latitude.

Atmos. Meas. Tech. Discuss., doi:10.5194/amt-2017-64, 2017
Manuscript under review for journal Atmos. Meas. Tech.
Discussion started: 5 April 2017

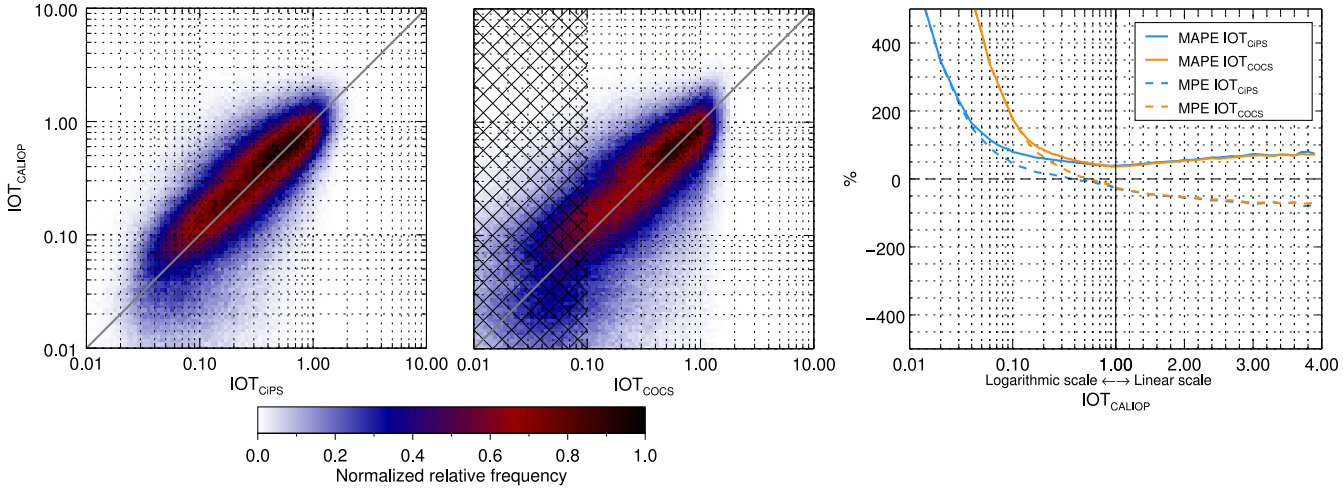

Figure 10. (Left) Density scatter plots with the IOT retrieved by CiPS and (centre) COCS (centre) on the horizontal axes and the corresponding V3 CALIOP data on the vertical axes. The grey lines represent the 1-1 line. (Right) The MAPE (solid) and MPE (dash) of the IOT retrieved by CiPS and COCS with respect to the IOT retrieved by CALIOP.

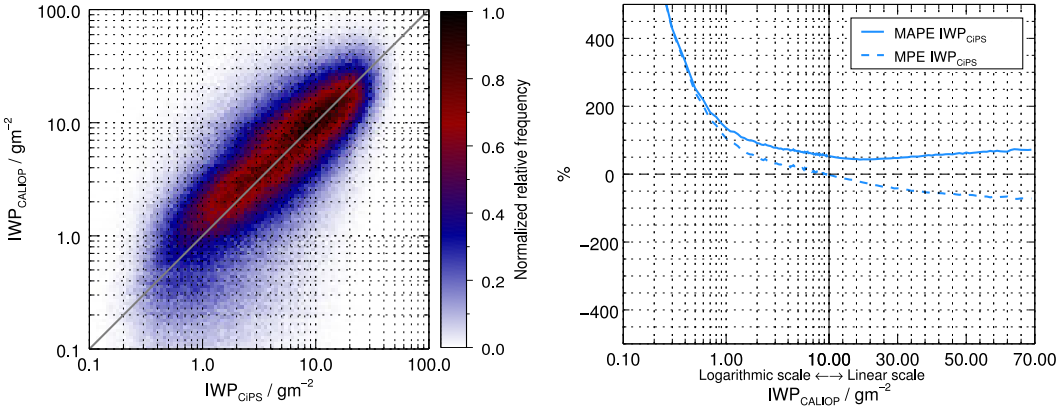

Figure 11. (Left) Density scatter plot with the IWP retrieved by CiPS on the horizontal axis and the corresponding V3 CALIOP data on the vertical axis. The grey line represents the 1-1 line. (Right) The MAPE (solid) and MPE (dash) of the IWP retrieved by CiPS with respect to the IWP retrieved by CALIOP.

Atmos. Meas. Tech. Discuss., doi:10.5194/amt-2017-64, 2017
Manuscript under review for journal Atmos. Meas. Tech.
Discussion started: 5 April 2017

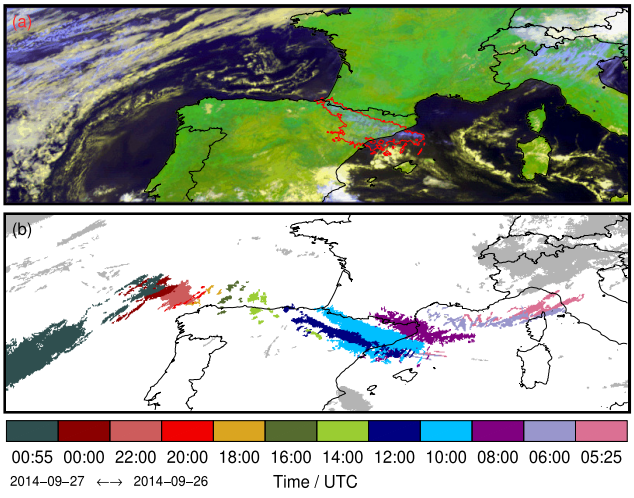

Figure 12. (a) False color RGB composite on September 26, 2014 at 10.00 UTC. The red contour of the CiPS cirrus cloud mask shows the outline of the cirrus cloud, whose life cycle is analysed. The orographic cirrus is clearly seen south of the Alps. (b) The path and temporal evolution of the cirrus cloud as it is tracked backward and forward in time with a temporal resolution of 120 min. The light grey color shows all cirrus clouds present at 05.25 UTC that were not tracked in order to understand the origin of the analysed cirrus cloud.

Atmos. Meas. Tech. Discuss., doi:10.5194/amt-2017-64, 2017
Manuscript under review for journal Atmos. Meas. Tech.
Discussion started: 5 April 2017

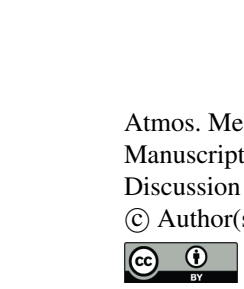

Atmospheric Measurement Techniques Discussions

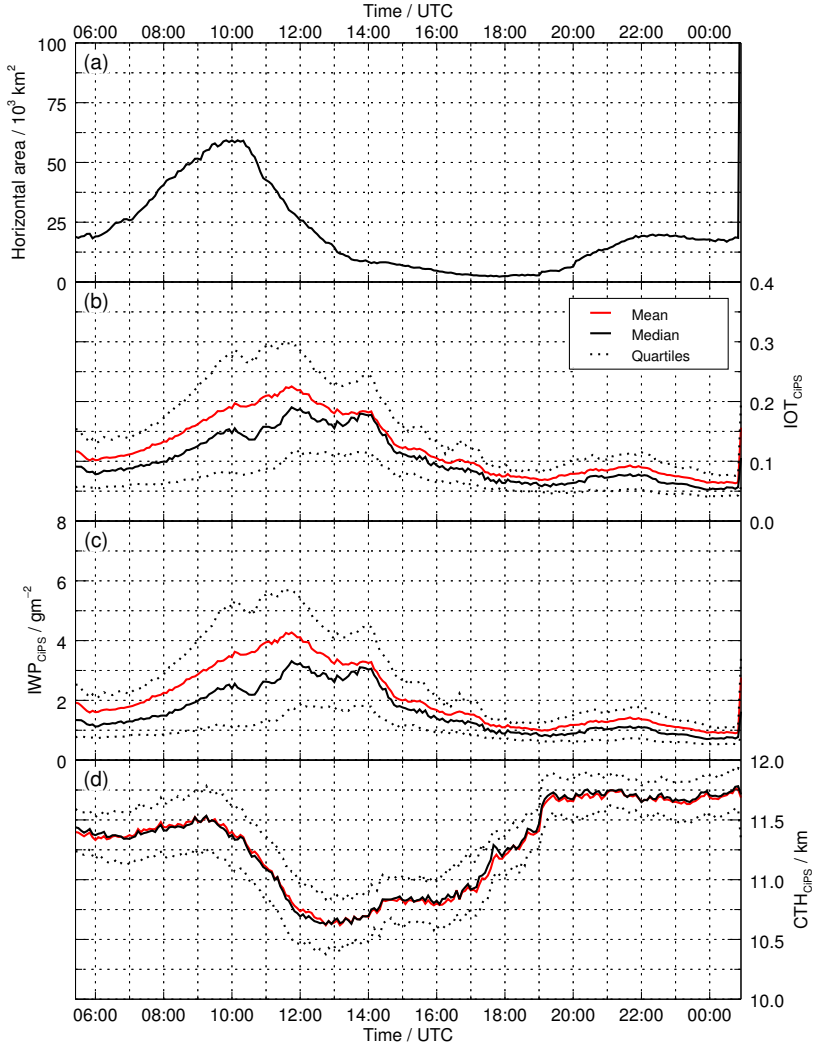

Figure 13. Temporal evolution of the cloud properties for the cirrus described in Fig. 12 with a temporal resolution of 5 min: (a) the horizontal cirrus cloud area, (b) IOT, (c) IWP and (d) CTH. For the IOT, IWP and CTH the mean, median, upper and lower quartile values are presented.